A low-dimensional Galerkin method for the three-dimensional flow around a circular cylinder

Bernd R. Noack and Helmut Eckelmann
Max-Planck-Institut für Strömungsforschung, Bunsenstr. 10, D-37073 Göttingen, Germany

(Received 30 December 1992; accepted 1 September 1993)

A low-dimensional Galerkin method for the three-dimensional flow around a circular cylinder is constructed. The investigation of the wake solutions for a variety of basic modes, Hilbert spaces, and expansion modes reveals general mathematical and physical aspects which may strongly effect the success of low-dimensional simulations. Besides the cylinder wake, detailed information about the construction of similar low-dimensional Galerkin methods for the sphere wake, the boundary-layer, the flow in a channel or pipe, the Taylor–Couette problem, and a variety of other flows is given.

I. INTRODUCTION

During the last decade, low-dimensional computational techniques for flow simulations have been an active field of research. These techniques are typically based on traditional Galerkin methods[1] with of the order of 100 global modes. These methods are ideally suited for gaining physical insight into the temporal dynamics and the motion of coherent structures,[2,3] for understanding the energy exchange mechanisms between small and large scales,[4] and for isolating the physical mechanisms involved in the transition.[5] A low-dimensional flow description may turn out to be a necessary prerequisite for global, three-dimensional (3-D) stability analyses,[6] since eigenproblems with of the order of many thousand numerical degrees of freedom are both numerically delicate and computationally expensive.

The global modes for the Galerkin methods may be derived in a mathematical, physical, or empirical manner. *Mathematical modes* typically arise from completeness considerations of function sets in a suitable separable Hilbert space (e.g., Lorenz's[7] treatment of the Rayleigh–Benard problem). *Physical modes* (e.g., Stokes or singular Stokes modes[8]) are generally chosen as eigenfunctions of related stability problems. *Empirical modes* require additional detailed experimental or numerical knowledge about the solution of the Navier–Stokes equation. The most prominent example of an empirical Galerkin method is the proper-orthogonal-decomposition (POD) technique.[9]

The present paper presents a mathematical Galerkin method which exploits and generalizes Zebib's[10] carrier-field ansatz for an incompressible velocity field. In Sec. II, this Galerkin method is constructed for the 3-D cylinder wake. It should be noted that this flow is one of the computationally most challenging flows with simple boundary conditions—because of the spatial inhomogeneity of the velocity field. The velocity field at moderate and large Reynolds numbers may roughly be decomposed in potential and boundary-layer flow besides a near-wake region which is dominated by nonlinear processes and a far-wake region which is governed by linear convection and dissipation mechanisms. All these different regions result from different physical processes which must be resolved by the Galerkin method and cannot be presupposed in the choice of the modes. In Sec. III, the properties of the Galerkin solutions for the cylinder wake are compared with other experimental and numerical investigations. In Sec. IV the advantages and disadvantages of the Galerkin method as compared to other simulation techniques are outlined. Then, general guidelines for successful Galerkin methods are developed (Sec. V). In particular, the influence of the basic mode, the Hilbert space, the mode properties, and the chosen subset of modes are investigated. In Sec. VI, possible generalizations of the presented Galerkin method for other flows are outlined.

II. CONSTRUCTION OF THE GALERKIN METHOD

A Galerkin method (GM) consists of a *kinematical* and *dynamical* part. In the kinematical part, the *Galerkin approximation* (GA), a finite Fourier expansion of the velocity field is constructed. This approximation is described in Sec. II A. In the dynamical part, the *Galerkin projection* (GP), the Navier–Stokes equation is projected to an evolution equation for the Fourier coefficients. The derivation of this evolution equation and its numerical realization is discussed in Sec. II B.

In the following, all quantities are assumed to be normalized with the cylinder radius R and the velocity U_∞. The dependent variables are expressed in terms of a cylindrical coordinate system (r,ϕ,z), where the cylinder is defined by $r=1$ and the oncoming flow is parallel to the $\phi=0$, ray in the $r\phi$ plane. The Reynolds number Re is based on the cylinder diameter.

A. Galerkin approximation

In this section, the solenoidal velocity field $\mathbf{u}$ at the position $\mathbf{x}$ and the time t is expressed as the sum of a *basic mode* $\mathbf{u}_0(\mathbf{x})$ and a linear combination of a finitely many—say N—*expansion modes* $\mathbf{u}_p(\mathbf{x})$ with time-dependent Fourier coefficients $a_p(t)$:

$$\mathbf{u}(\mathbf{x},t)=\mathbf{u}_0(\mathbf{x})+\sum_{p=1}^{N} a_p(t)\mathbf{u}_p(\mathbf{x}). \tag{1}$$

 1070-6631/94/6(1)/124/20/$6.00

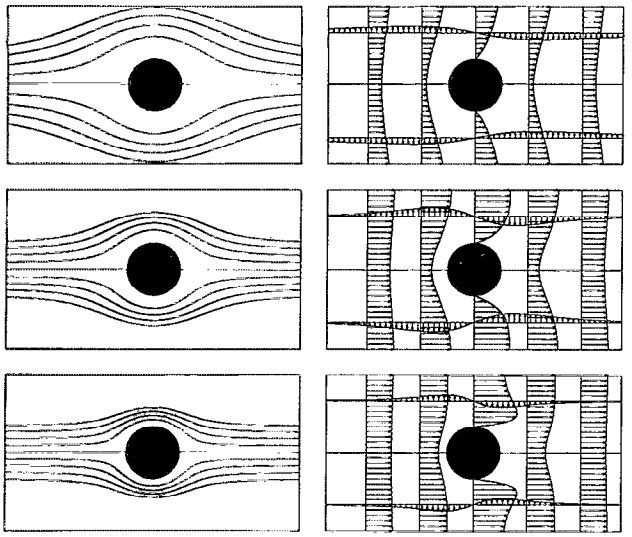

FIG. 1. Basic mode for Re=1 (top), Re=10 (middle), and Re=100 (bottom). In the left column, the streamlines are shown. In the right column, the velocity profiles $y \mapsto u(x,y)$ and $x \mapsto v(x,y)$ are displayed for $x=-4, -2, 0, 2, 4$, and $y=-2, 0, 2$, respectively.

This expression shall satisfy the boundary conditions (BC) at the cylinder and at infinity for all choices of the Fourier coefficients.

The basic mode essentially represents the oncoming flow. This mode can be taken from the two-dimensional (2-D) version of the GM:[11,12]

$$\mathbf{u}_0=\nabla\times\{\Psi_0\hat{\mathbf{e}}_z\}, \tag{2}$$

where $\hat{\mathbf{e}}_z$ represents the unit vector in z direction and Ψ_0 the streamfunction $\Psi_0=(r-1/r)\{1-\exp[-(r-1)/\delta_{bm}]\}\times\sin\phi$ with $\delta_{bm}=a_{bm}/\sqrt{\mathrm{Re}}$. The requirement that the maximal slope of the boundary-layer profile[11,12] is $1/\sqrt{\mathrm{Re}}$ yields for the proportionality constant $a_{bm}=4$. This basic mode behaves like a boundary layer at the cylinder, approaches the potential solution at infinity, and is divergence free. Figure 1 shows this mode for three Reynolds numbers.

The difference $\mathbf{u}'=\mathbf{u}-\mathbf{u}_0$ may be considered as a *perturbation* due to the cylinder and is expressed by two *generalized streamfunctions* $\Psi^{(1)}$ and $\Psi^{(2)}$:

$$\begin{aligned}\mathbf{u}'&=\nabla\times\{\Psi^{(1)}\hat{\mathbf{e}}_z\}+\nabla\times\nabla\times\{\Psi^{(2)}\hat{\mathbf{e}}_z\}\\&=\left(\frac{1}{r}\frac{\partial\Psi^{(1)}}{\partial\phi}+\frac{\partial^2\Psi^{(2)}}{\partial r\partial z}\right)\hat{\mathbf{e}}_r+\left(-\frac{\partial\Psi^{(1)}}{\partial r}+\frac{1}{r}\frac{\partial^2\Psi^{(2)}}{\partial\phi\partial z}\right)\hat{\mathbf{e}}_\phi\\&\quad-\Delta_{2D}\Psi^{(2)}\hat{\mathbf{e}}_z,\end{aligned} \tag{3}$$

where $\Delta_{2D}=\partial^2/\partial r^2+(1/r)(\partial/\partial r)+(1/r^2)(\partial^2/\partial\phi^2)$ is the 2-D Laplace operator. For 2-D flow, $\Psi^{(2)}$ vanishes identically and $\Psi^{(1)}$ represents the conventional streamfunction. For the 3-D flow, this expression is a general ansatz for an incompressible velocity field and has been suggested by Zebib.[10] The no-slip condition at the cylinder is enforced by requiring

$$\Psi^{(1)}=\frac{d}{dr}\Psi^{(1)}=\Psi^{(2)}=\frac{d}{dr}\Psi^{(2)}=\frac{d^2}{dr^2}\Psi^{(2)}=0 \tag{4}$$

at $r=1$. At infinity, the perturbation $\mathbf{u}'$ vanishes. This condition can be achieved by

$$\Psi^{(1)},\Psi^{(2)}\to 0 \quad \text{for } r\to\infty. \tag{5}$$

This limit is to be carried out on any ray $\phi=\text{const}\neq 0$. The asymptotic behavior of the generalized functions at infinity and its implication for the GM are discussed in the Appendix. In addition, we assume an L periodicity in spanwise direction

$$\begin{aligned}\Psi^{(1)}(r,\phi,z)&=\Psi^{(1)}(r,\phi,z+L),\\\Psi^{(2)}(r,\phi,z)&=\Psi^{(2)}(r,\phi,z+L),\end{aligned} \tag{6}$$

as in other recent 3-D cylinder wake simulations.[13,14] Then, the domain of the dependent variables can be restricted to

$$\Omega=[(r,\phi,z):\ r\geqslant 1,|z|\leqslant L/2].$$

It should be noted that $\Psi^{(\kappa)}$ ($\kappa=1,2$) are not elements of the space of square-integrable functions on Ω, $\mathscr{L}^2(\Omega)$, as shown in the Appendix. Yet, these generalized streamfunctions can be embedded in the weighted space $\mathscr{L}^2_\sigma(\Omega)$ with the weight $\sigma=r^{-\alpha}$ where $\alpha>0$ is a so far undetermined exponent. The inner product of f, $g\in\mathscr{L}^2_\sigma(\Omega)$ is defined by the volume integral over Ω

$$\begin{aligned}(f,g)_\Omega&=\frac{1}{L}\int_\Omega dV\, r^{-\alpha}fg\\&=\frac{2\pi}{L}\int_1^\infty dr\int_{-\pi}^{+\pi}d\phi\int_{-L/2}^{+L/2}dz\, r^{1-\alpha}fg,\end{aligned} \tag{7}$$

where the factor $1/L$ has been introduced for mathematical convenience.

The right choice of α is crucial for the success for the GM. If the Hilbert-space parameter α is too large, the weight vanishes too quickly in the wake region and the GM only resolves the boundary-layer physics. If, on the other hand, α is too small, the generalized streamfunctions for the asymptotic wake solutions are not an element of $\mathscr{L}^2_v(\Omega)$ anymore, since their norms diverge. In the present GM, we take the borderline parameter

$$\alpha=3/2. \tag{8}$$

This value is derived in the Appendix.

The BC at the cylinder defines two subspaces of $\mathscr{L}^2_\sigma(\Omega)$ for $\Psi^{(\kappa)}$, $\kappa=1,2$:

$$\mathscr{H}^{(1)}=\left\{\Psi\in\mathscr{L}^2_\sigma(\Omega):\ \Psi=\frac{d}{dr}\Psi=0 \quad \text{for } r=1\right\},$$

$$\mathscr{H}^{(2)}=\left\{\Psi\in\mathscr{L}^2_\sigma(\Omega):\ \Psi=\frac{d}{dr}\Psi=\frac{d^2}{dr^2}\Psi=0 \quad \text{for } r=1\right\}.$$

The form of the inner product (7) and the boundary condition (4) suggests to express the expansion mode $\Psi^{(\kappa)}_{ijk}$ of $\mathscr{H}^{(\kappa)}$ as the product of a *radial mode* $R^{(\kappa)}_i(r)$, an *azimuthal mode* $\Phi_j(\phi)$, and a *spanwise* mode $Z_k(z)$:

$$\Psi_{ijk}^{(\kappa)}(r,\phi,z)=R_i^{(\kappa)}(r)\Phi_j(\phi)Z_k(z). \tag{9}$$

The radial modes must depend on κ, since the boundary condition explicitly depends on κ, too.

The modes $\{\Psi_{ijk}^{(\kappa)}\}_{ijk}$ can be constructed to be a complete, countable orthonormal system (CCONS) of $\mathcal{H}^{(\kappa)}$ by requiring similar properties of the radial, azimuthal, and spanwise modes in the corresponding one-dimensional (1-D) function spaces. The radial modes $\{R_i^{(\kappa)}\}$ are thus supposed to be a CCONS of the space

$$\mathcal{R}^{(\kappa)}=\left\{R\in\mathcal{L}^2_{\sigma_{\mathcal{R}}}([1,\infty)):\ R(r)\right.$$
$$=\frac{d}{dr}R(r)=\cdots$$
$$\left.=\frac{d^\kappa}{dr^\kappa}R(r)=0\quad\text{for } r=1\right\}$$

with the weight $\sigma_{\mathcal{R}}=r^{1-\alpha}$ and the inner product $(f,g)_{\mathcal{R}}=\int_1^\infty dr\ \sigma_{\mathcal{R}}fg$ for $f,g\in\mathcal{R}^{(\kappa)}$. Analogously, the set of azimuthal modes $\{\Phi_j\}$ is required to be a CCONS of the space Φ of 2π-periodic functions with the inner product $(f,g)_\Phi=\int_{-\pi}^{\pi}d\phi\ fg$ for $f,g\in\Phi$. Similarly, $\{Z_k\}$ is chosen to be a CCONS in the space of L-periodic functions $\mathcal{Z}$, the inner product for $f,g\in\mathcal{Z}$ being defined by $(f,g)_{\mathcal{Z}}=(2\pi/L)\int_{-L/2}^{+L/2}dz\ fg$. Then, the expansion modes in $\mathcal{H}^{(\kappa)}$ are also complete and satisfy the orthonormality relationship

$$[\Psi_{ijk}^{(\kappa)},\Psi_{lmn}^{(\kappa)}]_\Omega=\delta_{il}\delta_{jm}\delta_{kn}$$

with the Kronecker symbol $\delta_{\mu\nu}=1$ for $\mu=\nu$ and $\delta_{\mu\nu}=0$ otherwise.

The radial modes can be constructed from the CCONS of $\mathcal{L}^2([0,\infty))$. This basis consists of Laguerre functions $S_i(x)=L_i(x)e^{-x/2}$, where L_i is a Laguerre polynomial of degree i and $i=0,1,2,\ldots$. Since the interval is infinite, the scaled Laguerre functions $\tilde{S}_i(x)=(1/\sqrt{\delta})S_i(x/\delta)$ $(\delta>0)$ also represent a CCONS. This freedom will turn out to be crucial for the success of the GM. Multiplying the scaled Laguerre functions with $1/\sqrt{\sigma_{\mathcal{R}}}$ and shifting the origin by one unit, we obtain the scaled modified Laguerre functions $R_i=1/\sqrt{\delta}r^{(\alpha-1)/2}L_i[(r-1)/\delta]\exp[(r-1)/2\delta]$, which represent the CCONS of $\mathcal{L}^2_{\sigma_{\mathcal{R}}}([1,\infty))$. A basis of $\mathcal{R}^{(\kappa)}$ with its BC at $r=1$ can be obtained from linear combinations of R_i. For an optimal resolution of the boundary layer and near wake, we introduce two scales $\delta^{(\kappa)}$, one for each radial Hilbert space. The resulting radial modes are

$$R_i^{(\kappa)}=\frac{1}{\sqrt{\delta^{(\kappa)}}}r^{(\alpha-1)/2}\left(\frac{r-1}{\delta^{(\kappa)}}\right)^{\kappa+1}P_i^{(\kappa)}\left(\frac{r-1}{\delta^{(\kappa)}}\right)$$
$$\times\exp\left[-\left(\frac{r-1}{2\delta^{(\kappa)}}\right)\right], \tag{10}$$

where $P_i^{(\kappa)}$ represents a polynomial of ith degree. The $\delta^{(\kappa)}$-independent coefficients of $P_i^{(\kappa)}$ are determined from a successive Gram–Schmidt orthonormalization of $R_0^{(\kappa)}$, $R_1^{(\kappa)}$, $R_2^{(\kappa)}$, $\cdots$ with respect to the inner product $(,)_{\mathcal{R}}$. Figure 2 displays the radial modes for $\delta^{(\kappa)}\equiv 1$. Although

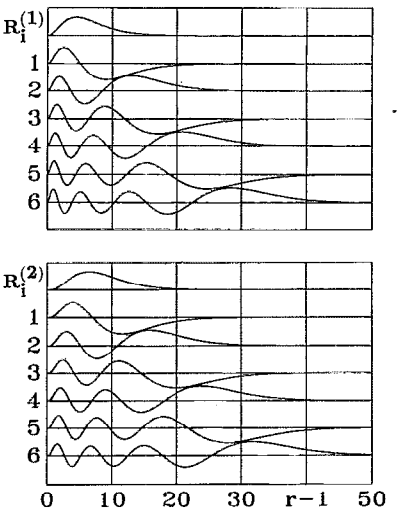

FIG. 2. The first radial modes for $\alpha=3/2$ and $\delta^{(\kappa)}\equiv 1$. The upper (lower) figure illustrates $R_i^{(\kappa)}$ for $i=0,1,\ldots,6$ from top to bottom and $\kappa=1$ ($\kappa=2$). The distance between two horizontal lines corresponds to an ordinate difference of 0.5, i.e., the extrema of all radial modes are in the range $(-0.3,+0.3)$.

the oscillatory behavior of these modes seems to be ideal for the description of the von Kármán vortex street, the boundary-layer resolution of the first modes is far too coarse. This deficit can be eliminated by suitable choices of the scales $\delta^{(\kappa)}$. A large $\delta^{(\kappa)}\sim 1$ implies a good resolution of the wake flow but a negligible resolution of the boundary layer. In contrast, a too small $\delta^{(\kappa)}$ yields a good approximation for boundary-layer structures but then the radial modes cover only a small portion of the wake. A good compromise for large Reynolds numbers seems to be a boundary-layer scaled parameter $\delta^{(\kappa)}=a^{(\kappa)}/\sqrt{\mathrm{Re}}$ with a suitable proportionality constant $a^{(\kappa)}$. For low Reynolds numbers, a minimal radial resolution may be guaranteed by removing the singularity at $\mathrm{Re}=0$ with a hyperbolic tangent:

$$\delta^{(\kappa)}=\tanh(a^{(\kappa)}/\sqrt{\mathrm{Re}}). \tag{11}$$

For large Re, this expression is still proportional to $\mathrm{Re}^{-1/2}$, while for $\mathrm{Re}\to 0$ we obtain $\delta^{(\kappa)}\to 1$.

The proportionality constants $a^{(\kappa)}$ are chosen in order to guarantee a minimal boundary-layer resolution due to the radial mode with the largest order i. In the present paper, this order is $I^{(\kappa)}=6$ for $\kappa=1,2$. First, we determine $a^{(1)}$. The arc from the stagnation point $\phi=180°$ and the "top" $\phi=90°$ has the length $\pi/2$. (Remember that all quantities are assumed to be normalized with the cylinder radius R and the velocity at infinity U_∞.) The potential flow assumes a velocity of 2 at the top. The displacement thickness at the end of a plate with the same length $\pi/2$ in a flow with the velocity 2 is, according to Blasius, given by $\delta_1=1.72\sqrt{\pi/2\mathrm{Re}}$. In this expression, the fact that the Reynolds number is based on $D=2R$ and not R as a reference scale has been taken into account. On the other hand, Eq. (3) yields for the tangential velocity profile due to $\Psi^{(1)}$: $u_\phi=-(d/dr)\Psi^{(1)}$. The first zero $r_1^{(1)}$ of $(d/dr)R_{I(1)}^{(1)}$ is

expressed by $r_1^{(1)}-1=0.879\delta^{(1)}$. Equating this boundary-layer resolution of the expansion mode with the estimate for the boundary-layer thickness, i.e., setting $r_1^{(1)}-1=\delta_1$, yields $0.879\delta^{(1)}=1.72\sqrt{\pi/2\mathrm{Re}}$. Hence, the proportionality coefficient in $\delta^{(1)}=a^{(1)}/\sqrt{\mathrm{Re}}$ is given by $a^{(1)}=2.45$. With this value, a (hypothetical) boundary-layer profile with an extremum half-way between the cylinder and δ_1 can still be approximated by the modes. Thus the inflectional boundary-layer profile $n\mapsto u_\phi(r,\phi)$ near the separation point with an extremum roughly at $r-1=\delta_1$ can still be approximately described by the GA. This profile may be considered as the superposition of a linear combination of radial modes which describe the velocity extremum near $r-1=\delta_1$ and a contribution of the highest-order radial mode with an extremum halfway between $r=1$ and $r=1+\delta_1$ in the reverse direction and a zero near $r=1+\delta_1$. With this superposition the $(\partial/\partial r)u_\phi(r=1,\phi)=0$ property of the inflectional profile can be assured without significantly changing the position of the velocity overshoot near $r=1+\delta_1$.

Similarly, $a^{(2)}$ is determined. For 2-D flows, $\Psi_2\equiv 0$ and the choice for $a^{(2)}$ is immaterial. Hence, $a^{(2)}$ can be considered as a measure for the resolution of 3-D structures in the boundary layer. Since 3-D boundary-layer structures typically extend also in the potential flow, we require only that the 99% thickness $\delta_{99\%}=5.1\sqrt{\pi/2\mathrm{Re}}$ of the "equivalent plate" can be resolved. On the other hand, the u_ϕ component of a $\Psi^{(2)}_{I^{(2)}jk}$ mode coincides with the first zero $r_1^{(2)}-1=1.73\delta^{(2)}$ of $R^{(2)}_{I^{(2)}}$, according to Eqs. (3) and (9). Equating the boundary-layer estimate, $\delta_{99\%}$ with the maximal resolution of the leading expansion modes $1.73\delta^{(2)}$ yields $a^{(2)}=2.95$. Summarizing, we obtain

$$a^{(\kappa)}=\begin{cases}2.45 & \text{for } \kappa=1,\\ 2.95 & \text{for } \kappa=2.\end{cases} \tag{12}$$

With the above parameters the best agreement between the Galerkin solutions (GS) and experiments is obtained as compared to significantly smaller or larger values. Yet, there is some arbitrariness in the estimate for the boundary-layer thickness and in the choice of the resolution quantity. Hence, the derivation of (12) may also be considered as an *a posteriori* explanation for the optimal parameters. Equations (10)–(12) completely define the CCONS in the radial Hilbert space.

The canonical choice for the azimuthal modes is given by

$$\Phi_j(\phi)=\begin{cases}\dfrac{1}{\sqrt{\pi}}\sin(j\phi) & \text{for } j>0,\\ \dfrac{1}{\sqrt{2\pi}} & \text{for } j=0,\\ \dfrac{1}{\sqrt{\pi}}\cos(j\phi) & \text{for } j<0.\end{cases} \tag{13}$$

The choice of trigonometric functions as azimuthal modes is mathematically reasonable and used in many spectral 2-D cylinder-wake simulations. (See, for instance, Patel[15] or Zebib.[10]) For small Reynolds numbers with nearly symmetrical Stokes-like solutions, this choice is also physically reasonable. For large Reynolds numbers, however, the azimuthal resolution is needed more urgently in the wake and not in the potential flow in the front of the cylinder. In contrast, the mathematical resolution is uniform in all directions. For optimal resolution of the flow per azimuthal mode we introduce "distorted azimuthal modes" with an increased resolution near $\phi=0$, i.e., in the wake, and a decreased resolution near $\phi=180°$ in the front:

$$\Phi_j(\phi)=\begin{cases}[(1+\gamma\cos\phi)/\sqrt{\pi}]\sin[jh(\phi)] & \text{for } j>0,\\ [(1+\gamma\cos\phi)/\sqrt{2\pi}] & \text{for } j=0,\\ [(1+\gamma\cos\phi)/\sqrt{\pi}]\cos[jh(\phi)] & \text{for } j<0,\end{cases} \tag{14}$$

with the azimuthal coordinate transformation

$$h(\phi)=\phi+\gamma\sin\phi(1+\cos\phi). \tag{15}$$

For $\gamma=0$, Eqs. (13) and (14) are equivalent. For $\gamma>0$, the new azimuthal modes have a larger amplitude in the wake and the zeros near $\phi=0$ are close together. The parameter γ should be Reynolds-number dependent. A suitable choice is $\gamma\propto\tanh(\mathrm{Re}/100)$. For small $\mathrm{Re}\ll 100$, the original uniform azimuthal resolution is restored, while for large $\mathrm{Re}\gg 100$, a Reynolds-number independent resolution in the wake region is obtained. The proportionality constant is chosen to be the relative deficit $(I^{(1)}-J^{(1)})/I^{(1)}$ of the largest azimuthal order $J^{(1)}$ versus the radial order $I^{(1)}$ for the $\Psi^{(1)}$ modes. Then

$$\gamma=\frac{I^{(1)}-J^{(1)}}{I^{(1)}}\tanh\left(\frac{\mathrm{Re}}{100}\right). \tag{16}$$

Figure 3 illustrates the new azimuthal modes for three Reynolds numbers. This new set of azimuthal modes is only orthonormal and complete for $I^{(1)}=J^{(1)}$, i.e., $\gamma\equiv 0$. For $I^{(1)}\neq J^{(1)}$ this set is not orthonormal and the completeness cannot be guaranteed too. Yet, orthonormality may be restored by applying the Gram–Schmidt procedure. Since this has no effect to all physical observables predicted with the GM we shall not pause to do so. The possible loss of completeness of the expansion modes is expected to be crucial only for pathological 2π-periodic functions. For the wake flow, it is natural to assume that also the distorted trigonometric functions arbitrarily exactly describe the cylinder flow with sufficiently many modes. The fact that the completeness of the new azimuthal modes cannot be guaranteed for all square-integrable 2π-periodic functions is sweetened by the observation that the introduction of the new azimuthal modes approximately halves the number of necessary modes for a given accuracy. For a practically oriented mind this is a good treat. Yet, it should noted that a guaranteed complete system of modes can be restored with a balanced radial and azimuthal resolution, i.e., $I^{(1)}=J^{(1)}$, although the resulting Galerkin method is less efficient (see Secs. III and IV A).

The spanwise modes are defined by

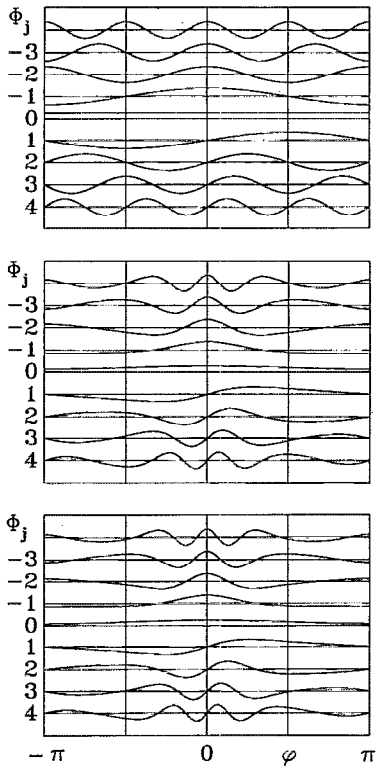

FIG. 3. The first azimuthal modes for $I^{(1)}=6$, $J^{(1)}=4$. The figures illustrates Φ_j, $j=-4,-3,...,3,4$ for Re=0 (top), Re=100 (middle), and Re=200 (bottom).

$$Z_k(z)=\begin{cases}1/\sqrt{\pi}\sin(2\pi kz/L) & \text{for } k>0,\\ 1/\sqrt{2\pi} & \text{for } k=0,\\ 1/\sqrt{\pi}\cos(2\pi kz/L) & \text{for } k<0.\end{cases} \tag{17}$$

It should be noted that the factor $1/L$ in Eq. (7) leads to L-independent scaling factors of the spanwise modes. In particular, the Z_0 mode neither depends on z nor on L. This implies that the Fourier coefficients of the 2-D wake are also solutions of the 3-D GM for all spanwise periods L.

The scalar expansion mode defined by Eq. (9) corresponds to a 3-D velocity field

$$\mathbf{u}_{ijk}^{(\kappa)}=(\nabla\times)^{\kappa}\{\Psi_{ijk}^{(\kappa)}\hat{\mathbf{e}}_z\}. \tag{18}$$

Therefore, the velocity can be approximated by

$$\mathbf{u}(\mathbf{x},t)=\mathbf{u}_0(\mathbf{x})+\sum_{\kappa=1}^{2}\sum_{ijk}a_{ijk}^{(\kappa)}(t)\mathbf{u}_{ijk}^{(\kappa)}(\mathbf{x}), \tag{19}$$

where $a_{ijk}^{(\kappa)}$ are time-dependent Fourier coefficients. Identifying a finite set of N quadruples (κ,i,j,k) with single indices p, Eqs. (1) and (19) are seen to be equivalent. In the following, the properties of the velocity modes $\mathbf{u}_{ijk}^{(\kappa)}$ are discussed and a selection of finitely many modes from an infinite set is proposed.

The 2-D flows, including the steady flow and the laminar von Kármán vortex street, are spanned by $\mathbf{u}_{ij0}^{(1)}$. Figures 4–6 display these 2-D modes for Re=0, Re=100, and Re=200, respectively. With increasing Reynolds number

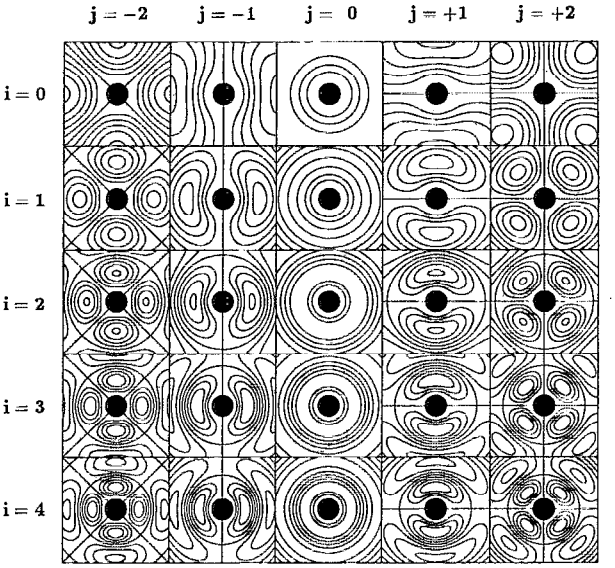

FIG. 4. Streamlines of the first 2-D expansion modes $\mathbf{u}_{ij0}^{(1)}$ for $I^{(1)}=6$, $J^{(1)}=4$, and Re=0.

the modes can be seen to "shrink" towards the cylinder and to "move" in the wake region. An example of a 3-D mode with $\kappa=1$ is illustrated in Fig. 7. For all these modes, the spanwise velocity component w vanishes identically, as can already be inferred from Eq. (3). In contrast, modes with $\kappa=2$ (see Fig. 8) typically generate fluid motion in spanwise direction.

Finally, a finite subset of modes is determined. For this subset, we limit the indices i, j, k for the modes $R_i^{(\kappa)}$, Φ_j, and Z_k by non-negative, κ-dependent integral numbers $I^{(\kappa)}$, $J^{(\kappa)}$, $K^{(\kappa)}$. The radial, azimuthal, and spanwise index subsets for i, j, and k are expressed by

$$\mathcal{I}^{(\kappa)}=\{0,...,I^{(\kappa)}\},$$

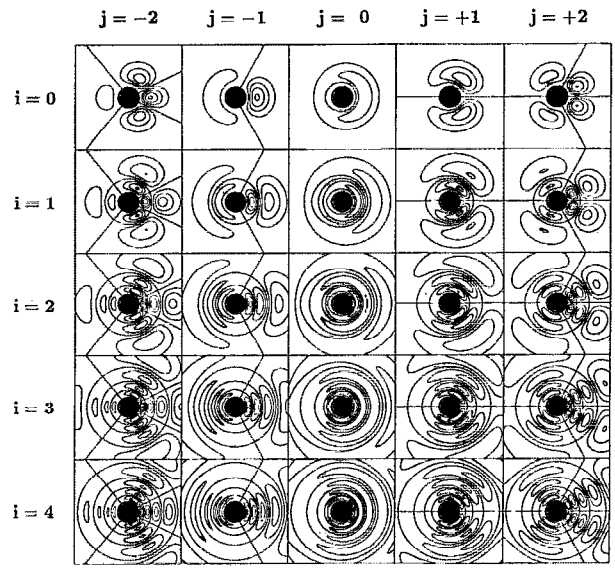

FIG. 5. Same as Fig. 4, but for Re=100.

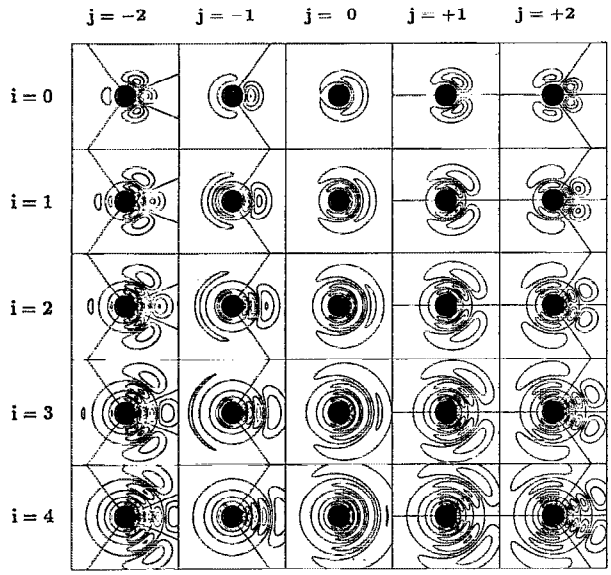

FIG. 6. Same as Fig. 4, but for Re=200.

$$\mathcal{J}^{(\kappa)}=\{-J^{(\kappa)},...,0,...,J^{(\kappa)}\},$$

and

$$\mathcal{K}^{(\kappa)}=\{-K^{(\kappa)},...,0,...,K^{(\kappa)}\},$$

respectively. For later reference, we define a subset of $\mathcal{K}^{(\kappa)}$

$$\mathcal{K}^{(\kappa+)}=\begin{cases}\{-K^{(\kappa)},...,0\} & \text{for } \kappa=1,\\ \{1,...,K^{(\kappa)}\} & \text{for } \kappa=2.\end{cases}$$

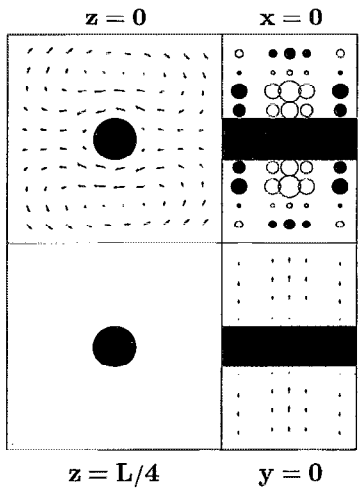

FIG. 7. Velocity field of $\mathbf{u}^{(1)}_{1,1,-1}$ with the parameters of Fig. 4 and $L=2\pi$. In the four pictures, the velocity fields in the planes $z=0$ (top, left), $z=L/4$ (bottom, left), $x=0$ (top, right), and $y=0$ (bottom, right) are illustrated. The arrows indicate the direction and magnitude of the velocity component in the considered plane. The diameters of the circles are proportional to the velocity component normal to this plane; the symbols are solid for positive and open for negative values. In the planes $z=0$, $z=L/4$, and $y=0$, the normal velocity component vanishes identically. The tangential component is zero in the planes $z=L/4$ and $x=0$.

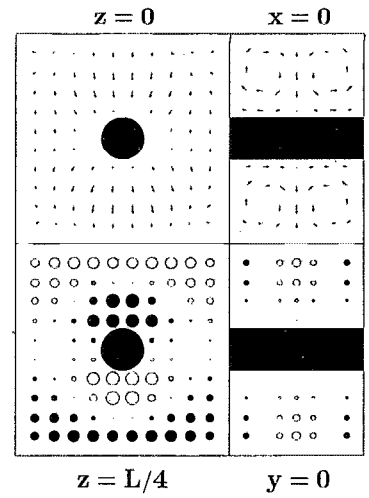

FIG. 8. Same as Fig. 7, but for $\mathbf{u}^{(2)}_{1,1,1}$.

The product ansatz (9) for the modes suggests to define the the product index set $\mathcal{J}_2=\mathcal{J}^{(1)}\times\mathcal{J}^{(1)}$ for the 2-D flow and $\mathcal{J}_3^{(\kappa)}=\mathcal{J}^{(\kappa)}\times\mathcal{J}^{(\kappa)}\times\mathcal{K}^{(\kappa)}$ for the 3-D case. In addition, we define $\mathcal{J}_3^{(\kappa+)}=\mathcal{J}^{(\kappa)}\times\mathcal{J}^{(\kappa)}\times\mathcal{K}^{(\kappa+)}$. With this notation, the indices i,j,k in Eq. (19) are summed over one of the above index sets. For simplicity, we set $I^{(1)}=I^{(2)}=I$, $J^{(1)}=J^{(2)}=J$, $K^{(1)}=K^{(2)}=K$, since there is no reason to maintain the κ dependency for the maximal radial, azimuthal, and spanwise index order. The "(κ)" superscript of the index sets can then be dropped. We are now enabled to define three finite-dimensional Hilbert spaces for the perturbation $\mathbf{u}'$, which are spanned by $\mathbf{u}^{(\kappa)}_{ijk}$. These spaces are $\mathcal{H}_{I,J}$ for 2-D simulations, $\mathcal{H}_{I,J,K}$ for general 3-D simulations, and $\mathcal{H}^{(+)}_{I,J,K}$, a subspace of $\mathcal{H}_{I,J,K}$ [which is invariant under the autonomous system (AS) (24) for $K=1$] for 3-D stability analyses:

$$\mathcal{H}_{I,J}=\text{span}\{\mathbf{u}^{(1)}_{ij0}:(i,j)\in\mathcal{J}_2\},$$

$$\mathcal{H}_{I,J,K}=\text{span}\{\mathbf{u}^{(\kappa)}_{ijk}:(\kappa,i,j,k)\in\{1,2\}\times\mathcal{J}_3\},$$

$$\mathcal{H}^{(+)}_{I,J,K}=\text{span}\{\mathbf{u}^{(\kappa)}_{ijk}:(\kappa,i,j,k)\in\{1,2\}\times\mathcal{J}_3^{(\kappa+)}\}.$$

The basis modes $\mathbf{u}^{(\kappa)}_{ijk}$ selected for each of these finite-dimensional Hilbert spaces are illustrated in Fig. 9.

B. Galerkin projection

In this section, an evolution equation for the Fourier coefficients in Eq. (1) is computed. This equation can be expressed as an autonomous system of ordinary differential equations, i.e., in the form

$$\frac{d}{dt}a_p=f_p(a_1,...,a_N)\quad\text{for } p=1,...,N, \tag{20}$$

where the functions f_p have to be derived from the Navier–Stokes equation.

We follow the guidelines given by Zebib.[10] In Sec. II A, the 3-D velocity field was expressed in terms of three functions Ψ_0, $\Psi^{(1)}$, $\Psi^{(2)}$. While Ψ_0 can be considered as a fixed point, only $\Psi^{(\kappa)}$ $(\kappa=1,2)$ are free and time-dependent

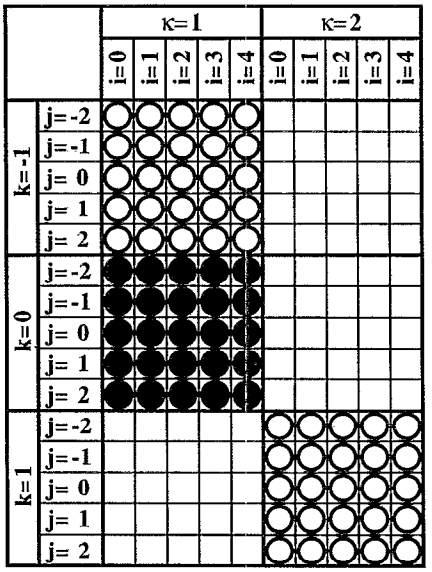

FIG. 9. Selected basis modes for the finite-dimensional Hilbert spaces. In the present example, the maximal radial, azimuthal, and spanwise orders are $I=4$, $J=2$, and $K=1$. Each of the 150 squares in the tableau corresponds to one mode $\mathbf{u}_{ijk}^{(\kappa)}$, where the index (κ,i,j,k) can be inferred from the corresponding row and column. The $\mathcal{H}_{4,2,1}$ space is spanned by all of the displayed modes. The basis modes of $\mathcal{H}_{4,2,1}^{\{+\}}$ are denoted by open or solid circles. The solid circles represent 2-D modes, which span the $\mathcal{H}_{4,2}$ space.

functions. Zebib expresses the incompressible Navier–Stokes equation as two coupled partial differential equations (PDE) for $\Psi^{(\kappa)}$ $(\kappa=1,2)$. (More precisely, Zebib derived two equations for $\Psi=\Psi_0+\Psi^{(1)}$ and $\Phi=\Psi^{(2)}$. He did not decompose Ψ in a basic mode and a perturbation.) For these PDEs, the 2-D and 3-D Laplace operators are introduced: $\Delta_{2D}=\partial^2/\partial r^2+(1/r)(\partial/\partial r)+(1/r^2)(\partial^2/\partial\phi^2)$, and $\Delta=\Delta_{2D}+\partial^2/\partial z^2$. Zebib's evolution equations resolved for the PDE-residua $R^{(1)}$ and $R^{(2)}$ read

$$
\begin{aligned}
0&=R^{(1)}(\Psi^{(1)},\Psi^{(2)})\\
&=\frac{\partial}{\partial t}\Delta_{2D}(\Psi_0+\Psi^{(1)})-\frac{2}{\mathrm{Re}}\Delta\Delta_{2D}(\Psi_0+\Psi^{(1)})\\
&\quad+\hat{\mathbf{e}}_z\cdot\nabla\times(\mathbf{u}\times\omega),
\end{aligned}
\tag{21}
$$

$$
\begin{aligned}
0&=R^{(2)}(\Psi^{(1)},\Psi^{(2)})\\
&=\frac{\partial}{\partial t}\Delta\Delta_{2D}\Psi^{(2)}-\frac{2}{\mathrm{Re}}\Delta^2\Delta_{2D}\Psi^{(2)}+\hat{\mathbf{e}}_z\cdot(\nabla\times)^2(\mathbf{u}\times\omega).
\end{aligned}
\tag{22}
$$

In this context, the velocity $\mathbf{u}$ and the vorticity ω are to be understood as abbreviations for $\nabla\times\{(\Psi_0+\Psi^{(1)})\hat{\mathbf{e}}_z\}+(\nabla\times)^2\{\Psi^{(2)}\hat{\mathbf{e}}_z\}$ and $(\nabla\times)^2\{(\Psi_0+\Psi^{(1)})\hat{\mathbf{e}}_z\}+(\nabla\times)^3\{\Psi^{(2)}\hat{\mathbf{e}}_z\}$, respectively.

With Zebib's evolution equations, the GP is a straightforward problem. First, $\Psi^{(\kappa)}$ $(\kappa=1,2)$ are replaced by the finite expansions $a_{ijk}^{(\kappa)}\Psi_{ijk}^{(\kappa)}$. In this and all following expressions, the *Einstein sum convention* is employed, i.e., two subscripts with the same index mean a summation over this index. In contrast, two superscripts (here: κ) do not imply a summation. Projecting the resulting Eqs. (21) and (22) on the expansion modes $\Psi_{ijk}^{(1)}$ and $\Psi_{ijk}^{(2)}$, respectively, yields

$$
[\Psi_{ijk}^{(\kappa)},R^{(\kappa)}(a_{lmn}^{(1)}\Psi_{lmn}^{(1)},a_{pqs}^{(2)}\Psi_{pqs}^{(2)})]_\Omega=0. \tag{23}
$$

In this system of equations, the volume integrals, specified by the inner product (7), are decomposed as linear combinations of products with three single integrals over r, ϕ, and z. These single integrals are computed numerically. Extracting the time derivatives of the Fourier coefficients $a_{ijk}^{(\kappa)}$ and identifying quadruple indices (κ,i,j,k) with single indices $p\in\{1,\ldots,N\}$ yields an evolution equation of the form (20):

$$
\frac{d}{dt}a_p=c_p+l_{pq}a_q+q_{pqs}a_qa_s. \tag{24}
$$

The coefficients for the constant, the linear and the quadratic term, c_p, l_{pq}, and q_{pqs}, respectively, represent volume integrals, which are independent of the Fourier coefficients.

Equation (24) is solved numerically using a predictor–corrector method recommended by Acton.[16] Clearly, the storage requirement and the computational efficiency of the GM is determined by the quadratic term in Eq. (24). The memory and computation time for this term can be decreased by a factor of approximately $\frac{1}{2}$ by introducing

$$
\tilde{q}_{pqs}=\begin{cases}q_{pqs}+q_{psq} & \text{for } q<s,\\ q_{pqs} & \text{for } q=s,\\ 0 & \text{for } q>s,\end{cases}
$$

and replacing $q_{pqs}a_qa_s$ by the equivalent expression $\tilde{q}_{pqs}a_qa_s$, where the summation is carried out only for $q\leqslant s$. In addition, the symmetry properties of the azimuthal and spanwise modes lead to many vanishing contributions to $\tilde{q}_{pqs}$. For the $\mathcal{H}_{6,4,1}^{\{+\}}$ GM with $N=189$ modes, only some 5% of the quadratic coefficients are nonvanishing. This fraction depends in a complicated manner on the index bounds I, J, K but tends to decrease with increasing N. Our present FORTRAN code exploits this "lacunary" with the sparse-matrix coding for all $N\times N$ matrices $(q_{pqs})_{qs}$ (for details see Noack[17]). Hence, the computation time of the GM increases less than with $O(N^3)$.

III. VALIDATION OF THE GALERKIN METHOD

In this section the validity of the Galerkin method (GM) is investigated. For this purpose the properties of the numerically computed flows are compared with published results. In particular, the steady flow (Sec. III A), its stability (Sec. III B), the 2-D periodic flow (Sec. III C), its stability (Sec. III D), and the asymptotically 3-D flow (Sec. III E) with its chaos-theoretical characterization (Sec. III F) are considered. If not otherwise stated the obtained results are based on the $\mathcal{H}_{6,4}$ Galerkin approximation (GA) for 2-D and the $\mathcal{H}_{6,4,1}^{\{+\}}$ GA for 3-D simulations.

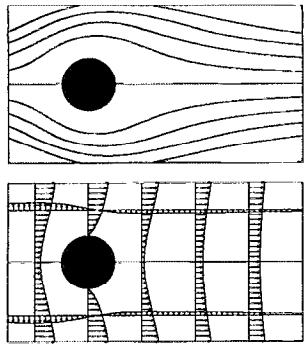

FIG. 10. Streamlines of the steady flow for Re=1. The flow is computed with a $\mathscr{H}_{6,4}$ GM.

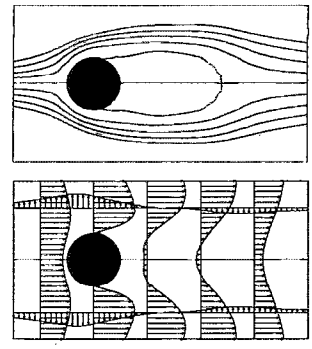

FIG. 12. Same as Fig. 10, but for Re=40.

A. Steady solution

Figure 10 shows the creeping flow for Re=1. The velocity field is symmetric with respect to the x axis but slightly asymmetric with respect to the y axis—in contrast to the basic mode (Fig. 1). This asymmetry increases with Re. At the Reynolds number of $\mathrm{Re}_{vp}=5$ the single separation point of the Galerkin solution (GS) bifurcates into a pair of symmetrical separation points and gives rise to a vortex pair (see Fig. 11). The value $\mathrm{Re}_{vp}=5$ coincides with the values given by other authors.[18] The length l_{vp} of the vortex pair, i.e., the distance from the saddle point to the rear point of the cylinder, increases nearly linearly with the Reynolds number. For Re=40 (see Fig. 12), the vortex length is 1.91 cylinder diameters which is in reasonably good agreement with the theoretical values of 2.24 by Fornberg[19] and 2.215 by Strykowski and Hannemann.[20]

All considered GAs exhibit qualitatively the same behavior. The "birth" of the vortex pair is predicted for $\mathrm{Re}_{vp}=5\pm1$; even the $\mathscr{H}_{2,2}$ GM with only six symmetrical expansion modes yields the correct value of 5 for Re_{vp}. The computed length of the vortex pair increases with the Reynolds number for all GMs (see Fig. 13). With increasing number of modes the predicted value of l_{vp} converges to the literature value of 2.2 at Re=40. For significantly larger Reynolds numbers the vortex lengths of the $\mathscr{H}_{4,4}$, $\mathscr{H}_{6,6}$, and $\mathscr{H}_{8,8}$ GMs are nearly constant. This saturation may be attributed to the finite azimuthal and radial resolution. If the GA expansions were somehow forced to describe a larger vortex pair, for instance by introducing a wake-centered weight function, this would probably lead to an unrealistic oncoming velocity field in the front. On the other hand, the $\mathscr{H}_{6,4}$ and $\mathscr{H}_{8,6}$ GAs can describe larger vortex pairs without significantly disturbing the oncoming flow because of the wake-centered azimuthal modes. Unfortunately there exist no experimental investigations about the unstable vortex pair at moderate Reynolds numbers and only little published numerical results, with which the present data can be compared.

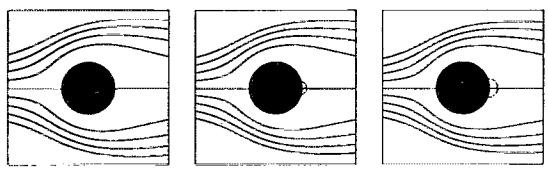

FIG. 11. Same as Fig. 10, but for Re=5 (left), Re=6 (middle) Re=7 (right).

B. Onset of periodicity

The steady solution becomes eventually unstable with increasing Reynolds number. The GM predicts a Hopf bifurcation with an isolated pair of eigenvalues.[11] This was anticipated by Sreenivasan, Strykowski, and Olinger[21] and can also be expected from theoretical considerations.[11] The corresponding critical Reynolds and Strouhal numbers are $\mathrm{Re}_{\mathrm{crit}}=53.3$ and $\mathrm{St}_{\mathrm{crit}}=0.148$. The critical Reynolds number exceeds Williamson's[22] experimentally and Jackson's[23] numerically obtained values of 47.8 and 45.4, respectively. The computed critical Strouhal number also exceeds Provansal, Mathis, and Boyer's[24] experimental value of 0.12 and Jackson's[23] result $\mathrm{St}_{\mathrm{crit}}=0.136$. The reason for this deviation is outlined in the following section. As expected, the discrepancy is reduced by increasing number of modes. With the $\mathscr{H}_{6,4}$ GM the experimentally obtained Landau model[21] for the supercritical Hopf bifurcation and its coefficients is reasonably well reproduced.[12]

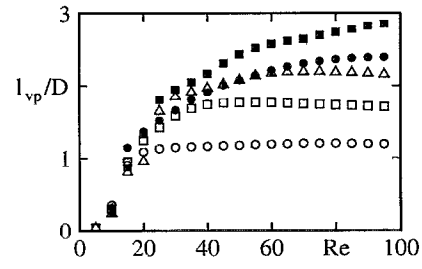

FIG. 13. Length of the vortex pair in terms of the Reynolds number for various Galerkin methods: open circles, $\mathscr{H}_{4,4}$ GM with $a^{(1)}=\sqrt{I^{(1)}}$ (see Noack and Eckelmann[11]); solid circles, $\mathscr{H}_{6,4}$ GM; open squares, $\mathscr{H}_{6,6}$ GM; solid squares, $\mathscr{H}_{8,6}$ GM; open triangles, $\mathscr{H}_{8,8}$ GM.

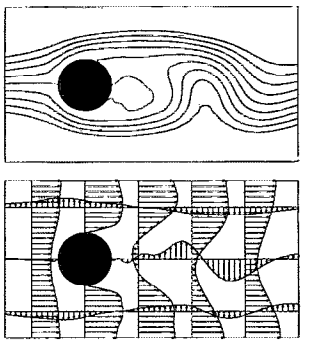

FIG. 14. Same as Fig. 10, but for an instant of the periodic flow for Re=100.

C. Periodic solution

Figure 14 shows the periodic GS for Re=100. The streamlines look similar to those of other simulations.[15] Yet, the theoretical Strouhal numbers (see solid circles in Fig. 15) significantly exceed the values obtained by Roshko's[25] formula St=0.212 (1−21.2/Re), particularly for large Reynolds numbers. This seems to be related with an insufficient far-wake resolution. The far wake can be considered as an "additional inertia" which slows down the "near-wake engine." The $\mathcal{H}_{6,4}$ GM does not resolve this inertia-effect properly, which explains why the theoretical Strouhal values are too large and not too small. By increasing the far-wake resolution of the GA, the deviation between experimental and theoretical frequencies can be significantly decreased. The Strouhal values of the $\mathcal{H}_{8,6}$ GS (solid squares in Fig. 15) lie much closer to the Roshko curve. "Stretching" the radial modes a bit further into the wake at the expense of the boundary-layer resolution[11,12] yields an even better agreement (stars in Fig. 15). The $\mathcal{H}_{6,6}$ GS (open squares) is less realistic than the $\mathcal{H}_{6,4}$ GS with less modes—probably for the reason mentioned in Sec. III A. The Strouhal frequencies of the 45 dimensional $\mathcal{H}_{4,4}$ GS (open circles) are obviously much too large.

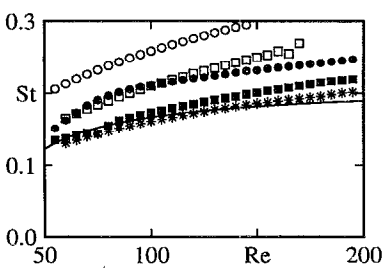

FIG. 15. Experimental and theoretical Strouhal–Reynolds-number relationship. The solid curve is the graph of Roshko's formula.[25] The symbols refer to numerical values obtained with various Galerkin methods: open circles, $\mathcal{H}_{4,4}$ GM with $a^{(1)} = \sqrt{I^{(1)}}$ (see Noack and Eckelmann[11]), solid circles, $\mathcal{H}_{6,4}$ GM; open squares, $\mathcal{H}_{6,6}$ GM; solid squares, $\mathcal{H}_{8,6}$ GM ($\gamma\equiv 0$); stars, $\mathcal{H}_{8,6}$ GM ($\gamma\equiv 0$ and $a^{(1)} = \sqrt{I^{(1)}}$, i.e., a further increased wake resolution).

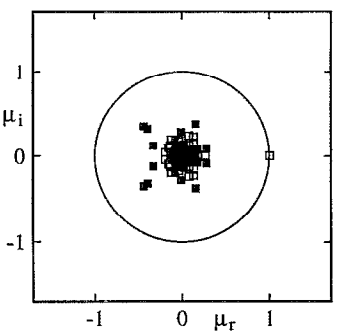

FIG. 16. Floquet spectrum for the critical point $\mathrm{Re}_{\mathrm{crit},2}=170$ and $k_{z,\mathrm{crit}} = 1.75$. Each square represents one (possibly complex) Floquet multiplier $\mu=\mu_r+i\mu_i$; a solid (open) symbol is associated with a 2-D (3-D) Floquet mode. For the numerical computation the $\mathcal{H}^{\{+\}}_{6,4,1}$ GM is chosen. For details see Refs. 6, 17, and 27.

D. Onset of three-dimensionality

The 2-D periodic flow becomes also eventually unstable with increasing Reynolds number. Experimental[26] and theoretical[13] investigations yield a 3-D instability which introduces a spanwise waviness. With the GM the first global stability analysis of this instability could be carried out.[27] The critical Reynolds number and the critical spanwise wave number is computed to be $\mathrm{Re}_{\mathrm{crit},2}=170$ and $k_{z,\mathrm{crit}} = 1.75$, respectively. At this critical point a positive Floquet multiplier, associated with a 3-D mode, leaves the unit circle (see Fig. 16) with increasing Reynolds number. The structure of the corresponding eigenmode indicates that the onset of three-dimensionality is caused by a near-wake instability (see Ref. 27). The critical Reynolds number deviates less than 5% from Williamson's[26] value of 178. Also, the critical spanwise wavelength of 1.8 diam is in good agreement with the experimentally obtained 1.7 diam by Noack, König, and Eckelmann.[27]

Figure 17 displays the stability diagram for the 2-D periodic solution. This stability diagram summarizes 35 Floquet analyses. The critical point $(\mathrm{Re}_{\mathrm{crit},2},k_{z,\mathrm{crit}})$ is the vertex of the parabola-shaped, thick neutral curve in Fig. 17. For $k_z\neq k_{z,\mathrm{crit}}$ the onset of three-dimensionality can be seen to occur at a higher Reynolds number. For $k_z=2$, the

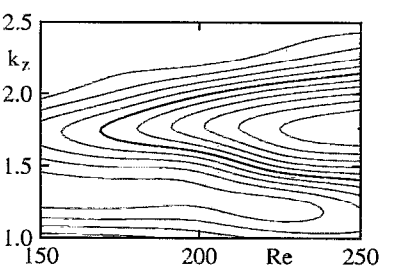

FIG. 17. Stability diagram for the onset of three-dimensionality. On each curve the spectral radius $|\mu_1(\mathrm{Re},k_z)|$ of the Floquet spectrum is a multiple of 0.1. The thick line represents the neutral stability curve $|\mu_1(\mathrm{Re},k_z)|=1$. The values of the spectral radius increase with Re for all considered fixed k_z. For the contour plot 35 Floquet analyses for Re =150, 175,..., 250 and k_z=1.0, 1.25,..., 2.5 have been carried out with the $\mathcal{H}^{\{+\}}_{6,4,1}$ GM. For details see Refs. 6, 17, and 27.

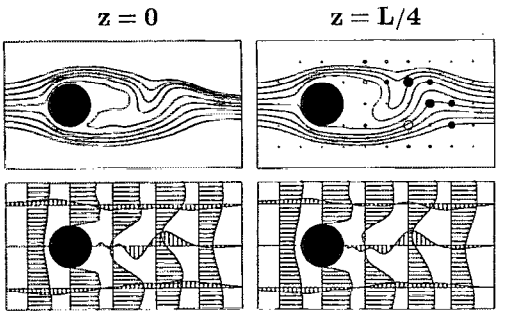

FIG. 18. Turbulent solution for Re=200, obtained with the $\mathscr{H}^{\{+\}}_{6,4,1}$ GM. The upper and lower rows display the instantaneous velocity field in the $z=0$ and $z=L/4$ plane. The curves in the left pictures are parallel to the x and y components of the velocity. The circles in the flow field are proportional to the spanwise velocity component; solid symbols denote positive, open ones negative spanwise components.

spanwise wave number used predominantly in the simulations of Karniadakis, Triantafyllou, and Tomboulides,[13,14] the critical Reynolds number is approximately 205 in good agreement with their value range 200–210 stated in Ref. 13.

There seems little doubt that the Galerkin model can describe the onset of three dimensionality. The relative deviation of the predicted critical point with experiments is even better than the discrepancy in the Strouhal number for the 2-D flow. Interestingly, 3-D vortex formations[28,29] can also be experimentally observed for $\mathrm{Re} < \mathrm{Re}_{\mathrm{crit},2}$. This three dimensionality can be explained in the framework of the Floquet analysis as an only neutral stability with respect to long wavelengths in spanwise direction.[27]

E. 3-D solution

After the onset of three dimensionality, a time-periodic 3-D flow for fixed $k_z=1.75$ and $170 < \mathrm{Re} < 200$ is observed. Such a flow has also been evidenced at a higher Reynolds number interval by Karniadakis and Triantafyllou[13] for a slightly different spanwise wave number. The Strouhal frequency St_{3D} of the asymptotic 3-D GS is lower than the corresponding frequency St_{2D} of the unstable 2-D periodic GS as was to be expected from Williamson's investigation.[26] We observe a supercritical transition from 2-D to 3-D shedding in agreement with the simulations of Karniadakis and Triantafyllou. Hence, the GM can describe the periodic 3-D flow at least qualitatively correctly with only $N=189$ modes. For finite-element accuracy of about 10% in the Strouhal number, in the velocity fields and other observables, a somewhat increased radial, azimuthal, and spanwise resolution is necessary.

The spatial structure of such a GS for Re=200 can be inferred from Fig. 18. The velocity field projected on the planes $z=$const essentially shows periodic vortex shedding and is nearly independent of z. The most intense spanwise velocity fluctuations are in the near-wake region, in agreement with the results of the Floquet stability analysis of Noack *et al.*[27] The vanishing spanwise velocity component in the $z=0$ plane is due to the symmetry properties of the expansion modes $\mathbf{u}^{(\kappa)}_{ijk}$ [$\kappa=1,2$, $(i,j,k)\in\mathscr{I}^{\{\kappa+\}}_3$] (see Figs. 7 and 8). The higher dimensional $\mathscr{H}_{6,4,1}$ GA with $N=378$ modes can also describe w fluctuations at any point in the flow region.

The period-doubling phenomenon, discovered numerically by Karniadakis, Triantafyllou, and Tomboulides,[13,14] is first observed in the Fourier spectra of the modes at $\mathrm{Re}\approx 280$. For the range $200 < \mathrm{Re} < 280$, the GM predicts a quasiperiodic flow with two similar frequencies—in contrast to other numerical simulations[13,14] at a somewhat larger wave number. With the presently available computer power it cannot be determined whether this quasiperiodicity is of physical origin, e.g., related to Williamson's[26] frequency jumps, or results from a truncation error of the GM in spanwise direction. Naturally, the $\mathscr{H}_{6,4,1}$ GM with the lowest possible spanwise resolution of $K^{(1)}=K^{(2)}=1$ cannot resolve the fine-scale structure on the von Kármán vortices observed by Williamson[26] for Re >260. In particular, no fully developed turbulent wakes can be reasonably modeled with of the order of 100 modes.

F. Dynamics of the nonperiodic, 3-D solution

For low-dimensional methods, it is generally of interest to determine the fraction of kinetic energy resolved by the modes, and the energy production and dissipation in terms of the dynamics in the mode space. In particular, the energy flux between small and large scales may yield additional insights in the dynamics of the flow and in possible truncation errors of the GM.

For the cylinder wake, however, both, the kinetic energy associated with the field $\mathbf{u}$ and with the perturbation $\mathbf{u}-\mathbf{u}_\infty$, ($\mathbf{u}_\infty$: velocity of the oncoming flow), is infinite in the considered domain Ω (see Sec. II A). In addition, the structures of the cylinder wake at moderate Reynolds numbers are dominated by only one scale, the cylinder diameter or, equivalently, the vortex size.

Nevertheless, some insight in the dynamics can be gained by computing the Lyapunov spectra and carrying out the Karhunen–Loewe decomposition of the attractor in the mode space. The Lyapunov spectrum $\{\gamma_n\}_{n=1}^{189}$ is calculated with a combined Wolf and Jacobi method. Figure 19(a) displays this spectrum for Re=300 and $k_z=1.75$. The spectrum contains one positive and one vanishing Lyaponov exponent, whereupon the remaining negative exponents decay linearly with the eigenmode index up to $n\approx 150$. This implies that the simulated flow is characterized by a strange attractor. Its correlation dimension can be estimated from the Lyapunov spectrum with the Kaplan–Yorke conjecture to be 3.41. This value is in good agreement with the correlation dimensions around 3.5 of constructed attractors from experimental velocity fluctuations.[30,31] This agreement suggests that at least the dynamics of the larger wake structures are qualitatively described by the GM. The true correlation dimension may be much larger taking the small-scale motion into account. Without the periodic boundary conditions in spanwise directions this dimension should even be infinite.

The strong decay of the Lyapunov exponents for $n>150$ corresponds well with Rempfer's[32] observation

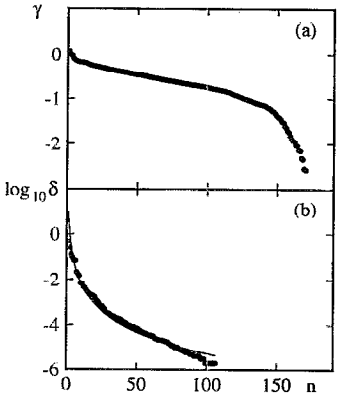

FIG. 19. Lyapunov spectrum $\{\gamma_n\}_{n=1}^{189}$ (a) and Karhunen–Loewe spectrum $\{\delta_n\}_{n=1}^{189}$ (b) for Re=300 and $k_z=1.75$. The solid curve in the δ_n data represents a power-law fit. The numerical computations are carried out with the $\mathscr{H}_{6,4,1}^{\{+\}}$ GM.

that his "turbulent viscosities" for the POD modes increase with their index. In his publication, this increase was attributed to a truncation effect at small scales.

The Karhunen–Loewe eigenvalues δ_n can be interpreted as the length of the nth principal axis of a Gaussian distribution fitted to the attractor. In case of 1-D motion, δ_1 is simply the standard deviation. Mathematically, δ_n is defined as the square-root of the nth (positive) eigenvalue of the correlation matrix. This matrix is computed from a sufficiently long trajectory around the mean value. This procedure is related to the Karhunen–Loewe procedure for the velocity fields with finite kinetic energies (see, for instance, Sirovich[33]), but is carried out in the mode space with obvious replacements for the correlation matrix "K_{ij}" (in Sirovich's notation) and the formulation of the eigenproblem formulation, etc.

Figure 19(b) displays the lengths δ_n of the principal attractor axes. These lengths decay approximately in proportion to $n^{-3.14}$. This strong decay indicates that the post-transient motion in the state space is essentially restricted to a low-dimensional manifold. Neglecting directions with $\delta_n<0.1\ \delta_1$ the dynamics is roughly confined in a six-dimensional subspace. This suggests that much more efficient GMs for the post-transient dynamics can, in principle, be constructed and that the present GM contains a large class of rapidly decaying transients. If, on the other hand, a large fraction of the eigenvalues δ_n would be of similar size, this may be considered as an indication that the mode expansion has not converged and that some basic properties of the post-transient flow may not be correctly resolved.

IV. APPLICABILITY OF THE GALERKIN METHOD

In this section the numerical and physical applicability of the Galerkin method (GM) is discussed. First, the convergence properties of the GM is investigated, including the validity of the low-dimensional model for 3-D physical processes in the wake region (Sec. IV A). Then the numerical efficiency (Sec. IV B) and the relative merits and disadvantages with respect to other computational techniques (Sec. IV C) are addressed.

TABLE I. Compilation of data for various Galerkin approximations (GA). From the left to the right column, the GA, the Reynolds number Re_{vp}, at which the separation point bifurcates into a vortex pair, the length l_{vp} of the vortex pair at Re=40, the critical Reynolds and Strouhal numbers, $\mathrm{Re}_{\mathrm{crit}}$ and $\mathrm{St}_{\mathrm{crit}}$, for the Hopf bifurcation, and the Strouhal values St for Re=100 and Re=200 are displayed, respectively. A "$\gamma=0$" superscript in the GA specification denotes that the azimuthal modes of Eq. (13) are chosen. A "*–np–*" entry at the Strouhal number indicates that the solution is not strictly time periodic. A Strouhal number in brackets represents St_1 of the stability analysis for the stable steady solution. The bottom row displays the corresponding literature values.

GA	Re_{vp}	l_{vp}/D	$\mathrm{Re}_{\mathrm{crit}}$	$\mathrm{St}_{\mathrm{crit}}$	St(100)	St(200)
$\mathscr{H}_{2,2}$	5	0.46	···	···	(0.303)	(0.196)
$\mathscr{H}_{4,4}$	5	2.12	···	···	*–np–*	*–np–*
$\mathscr{H}_{6,6}$	5	1.73	57.1	0.165	0.210	0.254
$\mathscr{H}_{8,8}$	4	1.98	62.6	0.172	0.219	0.302
$\mathscr{H}_{10,10}$	5	2.27	56.8	0.140	0.168	0.252
$\mathscr{H}_{4,2}$	3	1.08	42.0	0.211	0.200	0.232
$\mathscr{H}_{6,4}$	5	1.91	53.3	0.148	0.211	0.249
$\mathscr{H}_{8,6}$	6	2.16	55.7	0.166	0.238	0.294
$\mathscr{H}_{8,6}^{\gamma=0}$	4	1.72	52.4	0.133	0.173	0.223
Lit.	5	2.2	45.4	0.136	0.167	0.190

A. Convergence and physical structures resolved

In principle, the GM may be expected to approximately describe even the fully developed turbulent wake with an arbitrarily large amount of modes. This convergence property is implicitly assumed in all simulations with GMs of which the modes are based mathematical completeness considerations. Mathematically, however, this convergence is, as to the authors' knowledge, proven only for few 2-D GMs for closed flows.[34] In practice the amount of modes is restricted to a few hundred on a moderate workstation. In the following it will be outlined which physical processes can be properly described with a GM under this restriction.

The qualitative features of the 2-D steady and periodic flow may be captured with only 25 modes of the $\mathscr{H}_{4,2}$ GA. With 63 modes of the $\mathscr{H}_{6,4}$ GA this 2-D flow may also be described with an accuracy of the order of 10%. The Reynolds number range for which the present method can be applied is restricted to 300–400. With increasing Reynolds numbers the expansion modes shrink towards the cylinder and will eventually fail to resolve the wake region. This shortcoming may be circumvented by requiring a minimum value for the scaling parameters $\delta^{(1)}$ and $\delta^{(2)}$. Yet, no attempts have been made to improve the GM for higher Reynolds numbers.

The convergence properties for 2-D flows can be inferred from Table I. With increasing number of modes the numerical data become more realistic. In particular, the Strouhal frequencies for moderate Reynolds numbers improve. Yet for GMs with $I^{(1)}=J^{(1)}$ the convergence seems to be slow. Table I suggests that the convergence may be accelerated by choosing $I^{(1)}>J^{(1)}$ for the reasons mentioned in Secs. III A and III C.

TABLE II. Efficiency of the Galerkin method for various GAs. From left to right, the GA, the number of modes N, the CPU time t_{cpu} for 100 time steps on a SUNstation 2 in seconds, and the storage requirement S for Galerkin projection, respectively, is specified. This number of iterations corresponds approximately to one period of the von Kármán vortex street. S represents the amount of REAL*4 numbers for the storage of the quadratic term (in thousands).

GA	N	t_{cpu}(s)	S/1000
$\mathscr{H}_{2,2}$	15	0.1	0.4
$\mathscr{H}_{4,2}$	25	0.6	4.4
$\mathscr{H}_{4,4}$	45	1.3	7.9
$\mathscr{H}_{6,4}$	63	9.0	65.3
$\mathscr{H}_{6,6}$	91	6.3	49.1
$\mathscr{H}_{8,6}$	117	41.0	409.7
$\mathscr{H}_{8,8}$	153	19.5	185.9
$\mathscr{H}_{10,10}$	231	54.8	531.3
$\mathscr{H}^{(+)}_{2,2,1}$	45	1.3	6.1
$\mathscr{H}^{(+)}_{4,2,1}$	75	7.3	61.9
$\mathscr{H}^{(+)}_{4,4,1}$	135	12.8	118.1
$\mathscr{H}^{(+)}_{6,4,1}$	189	85.6	958.0

Referring to 3-D flows the $\mathscr{H}^{(+)}_{6,4,1}$ GM successfully describes the critical parameters of the onset of three-dimensionality. Even the only 75(!) dimensional $\mathscr{H}^{(+)}_{4,2,1}$ GM yields $\mathrm{Re}_{\mathrm{crit},2}=152.2$ and $k_{z,\mathrm{crit}}=1.72$. These data are in fairly good agreement with experiments. Hence, there is sufficient reason to believe that the spanwise waviness on the von Kármán vortices is reasonably described by the GM with less than 200 modes. The fine-scaled spanwise structures in the irregular Reynolds number range (Re >300) can, of course, not be resolved with several hundred modes. The validity of the low-dimensional 3-D GMs ends with the transitional Reynolds number range.

B. Efficiency

The efficiency of a computational technique for flow simulations is determined by two factors, the storage requirement and the amount of operations per time step. For the GM the storage requirement is essentially determined by the coefficients $\tilde{q}_{ijk}$ for the quadratic term. A naive implementation of the quadratic term would require N^3 REAL*4 numbers. Since most coefficients vanish this procedure would be very inefficient. By applying a simple storage technique for sparse matrices (see Noack[17]), the amount of coefficients to be stored is given by

$$S=\max_{i=1,\ldots,N}\ \mathrm{card}\{\tilde{q}_{ijk}:\ j=1,\ldots,N;\quad k=1,\ldots,N;\quad \tilde{q}_{ijk}\neq 0\},$$

where the "card" term denotes the number of the nonzero elements in the matrix $\{\tilde{q}_{ijk}\}_{jk}$. In Table II this storage requirement and the CPU time for the numerical integration is listed for various 2-D and 3-D GMs. The computational load for the 2-D and 3-D simulations of one shedding period is 9 s and 1.5 min on a SUNstation2, respectively, with the standard $\mathscr{H}_{6,4}$ and $\mathscr{H}^{(+)}_{6,4,1}$ GM. This is roughly two or three orders of magnitudes faster than traditional finite-difference or finite-element methods. Spectral-element methods (see, for instance, Karniadakis[35]) tend to be somewhat faster. For reasons of fairness it must be mentioned that grid and spectral-element method also compute the far wake, which is not resolved by the employed GMs.

The storage requirement can also be considered as small. Even the 3-D $\mathscr{H}_{6,4,1}$ GM needs only around one million of REAL*4 numbers, i.e., only 4 Mbyte RAM, and can conveniently be implemented on a modern personal computer.

It should be noticed that the storage requirement S is, in our sparse-matrix implementation, the operational count for the evaluation of the quadratic term and therefore proportional to the CPU time per time step. The number S depends in complicated manner on the chosen GA. It does not necessarily increase with the amount of modes N as Table II reveals. As a rule of thumb we get $S=0.25N^3$ for $\mathscr{H}_{KL}$ GMs with $K=L$, $S=0.50N^3$ for $\mathscr{H}_{KL}$ GMs with $K\neq L$, $S=0.05N^3$ for $\mathscr{H}^{(+)}_{KL1}$ GMs with $K=L$, and $S=0.15N^3$ for $\mathscr{H}^{(+)}_{KL1}$ GMs with $K\neq L$. The coefficients tend to decrease with increasing N.

C. Comparison with other numerical methods

In this section, the advantages and disadvantages of the presented GM is compared with high-dimensional grid-based computation techniques, like finite-difference, finite-element, and spectral-element methods.

The GM is an ideal tool for investigations where the asymptotical solutions and a sufficiently large class of transients need to be described in a comparatively low-dimensional state space. These investigation include global stability and chaos-theoretical analyses. As to the authors' knowledge our GM for the cylinder wake is presently the only available tool for carrying out global 3-D stability analyses of the steady flow (see König, Noack, and Eckelmann[36]), global 2-D and 3-D Floquet analysis of the periodic cylinder wake (see Noack, König, and Eckelmann[27]), and chaos-theoretical analyses of the non-periodic flow, like the determination of Lyapunov spectra, Karhunen–Loewe spectra, and estimates for the attractor dimension) (see Noack and Eckelmann[37]).

In addition the GM is a numerically very efficient solver for the 2-D flow and the 3-D near wake in the transitional Reynolds number range ($170<\mathrm{Re}<300$). This efficiency makes it an attractive method for parameters studies, for instance when a gross overview of some flow features for a large number of Reynolds numbers and spanwise wave numbers is desired.

The GM cannot compete with grid-based computational techniques for very accurate simulations of the velocity fields, for the resolution of far-wake properties, and for large-Reynolds-number simulations (2D and 3D). On the other hand grid-based methods are not well suited for global stability or chaos-theoretical analyses. As to the authors' knowledge only 2-D stability analysis of the steady flow,[10,23] yielding only the most critical eigenvalue and its eigenmode, have been carried out with grid-based methods.

Naturally, one can construct a variety of "hybrid" methods, where the knowledge of solutions from grid-based methods is exploited for the construction of low-dimensional models, e.g., POD techniques. This is the pre-

TABLE III. Phenomenogram data of Galerkin methods with different basic modes.

a_{bm}	Re_{crit}	St_{crit}	St(100)	St(200)
2	53.1	0.145	0.211	0.247
4	53.3	0.148	0.211	0.249
8	53.5	0.147	0.209	0.248

TABLE IV. Phenomenogram data of Galerkin methods with different Hilbert spaces.

α	Re_{crit}	St_{crit}	St(100)	St(200)
0	44.4	0.173	0.246	0.261
1.5	53.3	0.148	0.211	0.249
3	–e–	–e–	0.192	0.236

ferred approach when a given transient or a given post-transient flow is to be modeled as accurately and as low dimensional as possible. Thus the periodic 2-D cylinder wake can be described with only 8 POD modes.[38] This technique can provide valuable insights in the main physical processes of a given flow. Yet, this method is less suitable for stability analyses since the model can, by construction, describe only a small class of transients which may not contain the most important eigenmodes.

Summarizing the GM may not be the preferred numerical method for accurate flow simulations but has a variety of applications in which is far superior to other techniques, like stability and chaos-theoretical studies.

V. OTHER GALERKIN VARIANTS

The GS for the cylinder flow show that a reasonable wake simulation can be obtained with a comparatively low-dimensional Galerkin method (GM). This GM contains a variety of "ingredients", namely the basic mode, the Hilbert space, the azimuthal and radial modes besides the set of considered expansion modes. These ingredients may be chosen differently than suggested in Sec. II. In Secs. V A–V E, their influence on the GS is systematically investigated. These investigations elucidate which aspects are crucial for the success of the GM and which not. These results are expected to be valid for related GMs of other flows. Finally (Sec. V F) the possibility of constructing GMs on finite domains, which are typically used for the grids of finite-difference or finite-element methods, is outlined.

The discussion is restricted to 2-D flows with the $\mathcal{H}_{6,4}$ GM as a "reference point." The quality of the solution is judged from some phenomenogram data: the critical Reynolds number Re_{crit} for the onset of periodicity, the corresponding critical Strouhal number St_{crit}, as determined from a global stability analysis, besides the Strouhal frequencies St(100) and St(200) for the Reynolds numbers 100 and 200, respectively. For reasons of comparison, Jackson's[23] critical Reynolds and Strouhal number, $Re_{crit}=45.4$ and $St_{crit}=0.136$, and Roshko's[25] frequencies $St(100)=0.167$ and $St(200)=0.190$ are included in some comparisons.

A. Choice of the basic mode

Table III lists the phenomenogram data for half, the original, and twice the scaling parameter a_{bm} [see Eq. (2)] for the basic mode. The other parameters are held constant. The GS is hardly effected by the variation of a_{bm}. The expansion modes seem to compensate the variation of the basic mode. Yet, a variation of the basic mode may significantly affect the GS if the gradients of $\mathbf{u}_0$ are too large—say of the order of 10. These sharp gradients cannot be compensated by the expansion modes any more. Summarizing, *the success of the GM is insensitive to a reasonable choice of the basic mode.*

B. Choice of the Hilbert space

In Table IV, GS data for the Hilbert-space parameters $\alpha=0$, 1.5, and 3 are compiled. For $\alpha=0$, i.e., for the case that the Hilbert space does not contain the asymptotic solution, the frequencies are significantly too large. In addition, the velocity fields have little in common with the experimentally observed ones. For $Re<10$, the GS explodes for almost all initial conditions.

For $\alpha=3$, i.e., for the case that the GM essentially resolves the boundary-layer physics, the GS explodes for all moderate Reynolds numbers (denoted by "–e–" in the St column of Table IV). Only for larger Re values, physically acceptable periodic flows are generated. These solutions show that *the success of a GM for an open flow crucially depends on a physically motivated choice of Hilbert space.*

C. Choice of the radial modes

The resolution scale $\delta^{(1)}$ for the radial modes has an important impact on the success of the GM. For a Re-independent scale $\delta^{(1)}\equiv 1$, the GS explodes for all $Re>10$. For an increased number of azimuthal and radial modes, the explosion occurs even earlier.[39] This behavior has two reasons. The first reason is of kinematic nature. For sufficiently large Reynolds numbers, the boundary layer cannot be adequately resolved by the expansion modes any more. The second reason is related to the dynamics. For Re-independent modes, the magnitude of the Galerkin-projected dissipation term decreases in proportion to 1/Re at a given location in the mode space. Hence, the GP essentially describes a frictionless flow with no-slip conditions at the cylinder for sufficiently large Reynolds numbers. The resulting inviscid instability mechanism and the lack of an efficient damping process is responsible for the exploding GS. Therefore, *the asymptotic $1/\sqrt{Re}$ scaling of the radial modes is necessary for a successful, low-dimensional GM.* In fact, the boundary-layer scaled radial modes can be derived by requiring the same order of magnitude for the Galerkin representation of the convection and dissipation term in the mode space (see Noack and Eckelmann[12]).

The effect of the proportionality constant $a^{(1)}$ on the GS is less crucial, as can be inferred from Table V. Only if

TABLE V. Phenomenogram data of Galerkin methods with different radial modes.

$a^{(1)}$	Re_{crit}	St_{crit}	St(100)	St(200)
1	...	...	–s–	–s–
2	47.5	0.159	0.224	0.268
2.45	53.3	0.148	0.211	0.249
3	44.8	0.129	0.218	0.230
4	...	...	...	...

$a^{(1)}$ is much too small (here, $a^{(1)}=1$), the GS is steady for all considered Reynolds numbers (denoted by "–s–" in Table V), since the near-wake instability for the onset of periodicity cannot be adequately resolved. Choosing $a^{(1)}$ too large (here, $a^{(1)}=4$) leads to a nonperiodic or exploding GS, since the effect of dissipation is not adequately described by the AS.

D. Choice of the azimuthal modes

Table VI compares the phenomenogram data for the "conventional" azimuthal modes, defined by Eq. (13), and the actual ones, given by Eq. (14). For $Re<170$, the difference between the corresponding GSs is small. For larger Reynolds numbers, the flow of the GS with $\gamma\equiv 0$ becomes nonperiodic (denoted by "–np–" in Table VI). The nonperiodicity may be characterized by small chaotic fluctuations superimposed on a periodic motion. This undesirable behavior seems to result from an insufficient azimuthal resolution of the wake region, since increasing the azimuthal resolution J by 2 (i.e., using a $\mathcal{H}_{6,6}$ GM) yields a stable periodicity. For the present GM the nonperiodic behavior starts at much larger Reynolds numbers around 500. *Hence, the "distortion" of the trigonometric functions in Eq. (14) is not necessary for successful GMs, but it reduces the number of necessary expansion modes.*

E. Choice of the selected subset of modes

One expects the GSs to converge to the true solution with increasing number I and J of radial and azimuthal modes. For $I,J<8$, the truncation errors due to the finiteness of the expansion may become severe. Reasonable GSs may usually be obtained for the cases $I=J$ or $I=J+2$. For odd radial or azimuthal resolutions I, J, the GSs often exhibit nonphysical velocity fields or, if their qualitative behavior is reasonable, the phenomenogram data deviate intolerably from the values in the literature. This truncation effect diminishes rapidly for $I,J\gtrsim 8$, when the coefficients of the high-order contributions become small.

TABLE VI. Phenomenogram data of Galerkin methods with different azimuthal modes.

γ	Re_{crit}	St_{crit}	St(100)	St(200)
0	44.4	0.155	0.205	–np–
Eq. (16)	53.3	0.148	0.211	0.249

TABLE VII. Phenomenogram data for low-dimensional Galerkin methods with an increased wake resolution ($a^{(1)}=2.45\sqrt{I/6}\approx\sqrt{I}$). The set of considered modes is specified in the GA column. The Strouhal values in brackets are the critical frequencies obtained with a global stability analysis of the steady solution.

GA	Re_{crit}	St_{crit}	St(100)	St(200)
$\mathcal{H}_{2,2}$	...	...	(0.275)	(0.252)
$\mathcal{H}_{4,2}$	50.6	0.196	0.197	0.229
$\mathcal{H}_{4,4}$	42.0	0.184	0.259	0.330
$\mathcal{H}_{6,4}$	53.3	0.148	0.211	0.249

Table I displays the phenomenogram data for some $I=J$ and $I=J+2$ cases. For the $\mathcal{H}_{2,2}$ GM, the asymptotic solution remains steady for all Reynolds numbers. For $\mathcal{H}_{4,4}$ GM, the asymptotic solutions for $Re=100$ and 200 display a dominant periodicity with small nonperiodic fluctuations. For the other GMs, the phenomenogram is at least qualitatively correct. Quantitatively, however, the data partly deviate considerably from the values in the literature and convergence is not reached. Yet, it must be recalled that the present GM needs only a small fraction of the numerical degrees of freedom typically required for wake simulations. Finite-difference methods are carried out with about 10 000 grid points, which is more than two orders of magnitudes larger. In view of the number of modes, the GMs yield very reasonable results.

For a quick qualitative inquiry of the periodic solutions and its transients, the GM may be improved by an increased $a^{(1)}=2.45\sqrt{I/6}\approx\sqrt{I}$ for $I\leqslant 6$. This scaling parameter guarantees a minimal boundary-layer resolution for *each* maximal radial order I (see Noack and Eckelmann.[11] Table VII presents the corresponding phenomenogram data. Periodic vortex shedding can already be obtained with the $\mathcal{H}_{4,2}$ GM with 25(!) expansion modes.

F. Galerkin approximation on finite domains

The GM fulfills, by construction, the exact boundary conditions at infinity. In contrast, grid-based computational techniques resolve the cylinder wake in finite domains, for instance, a half-circle in the front joined with long rectangle in the wake region (see, for instance, Ref. 13). Typically, the boundary conditions at infinity are enforced at the outer grid boundaries except for the wake region. Inside the wake, no uniform flow can be assumed. Instead, various outflow conditions, like the mixed Neumann/viscous-sponge condition,[13,40] are in use.

With the construction of a GM on a *finite* domain the problem with the infinite norms for $\alpha=0$ could be circumvented. Yet, this at the first sight attractive approach may give rise to severe methodological and physical problems. The mathematical simplicity of the present GM rests on the product Hilbert space character, i.e., the construction of expansion modes from three complete function systems for each coordinate, r, ϕ, and z. This separation of coordinates cannot easily be restored, in part due to the different kind of conditions at the outer boundary of the finite domain. Even if a complete system of expansion modes on the

finite domain can be constructed, the infinite norm problem will reoccur in a different manner. Then the GSs will probably strongly depend on the chosen dimensions of the domain. The GP can be expected to "neglect" the boundary-layer physics and the flow in the front of the cylinder if, for instance, the area of the rectangle in the wake region is much larger than the area of the half-circle in the front. For flows in more complex geometries, like this one, Karniadakis'[8] singular Stokes modes seem to be a more flexible and promising route.

VI. GENERALIZATION TO OTHER FLOWS

At first sight, the GM presented in the previous sections seems to be restricted to the circular cylinder in uniform flow. Yet, with minor modifications this method can be applied to a large variety of other flow problems. In the following, the complete information for the construction of the GMs for a circular cylinder in shear and periodic flow (Secs. VI A and VI B), for the wake behind a sphere (Sec. VI C), for the boundary layer (Sec. VI D), channel (Sec. VI E), and pipe flow (Sec. VI F), and for the Taylor–Couette problem (Sec. VI G) is given. These GMs are to be understood as untested suggestions, which are expected to yield approximate solutions to the Navier–Stokes equation for sufficiently large number of modes, but may need to be modified for a successful low-dimensional simulation. In addition (Sec. VI H), the applicability of the method for complex geometries is discussed.

A. Circular cylinder in shear flow

The GM may easily be applied to the circular cylinder in shear flow by modifying the basic mode. The Hilbert spaces for the generalized streamfunctions $\Psi^{(1)}$, $\Psi^{(2)}$ and the expansion modes $\Psi_{ijk}^{(\kappa)}$ need not to be changed.

A suitable basic mode is given by

$$\Psi_0=\left(r-\frac{1}{r}\right)\left[1-\exp\left(-\frac{r-1}{\delta_{bm}}\right)\right]\sin\phi+\frac{1}{2}a\left(r^2-\frac{1}{r^2}\right)\times\left[1-\exp\left(-\frac{r-1}{\delta_{bm}}\right)\right]\sin^2\phi,$$

where a is the shearing parameter. For $a=0$, i.e., no shear in the oncoming flow, the original GM is restored. For arbitrary a, the basic mode $\mathbf{u}_0=\nabla\times\{\Psi_0\hat{\mathbf{e}}_z\}$ converges rapidly to $(1+ay)\hat{\mathbf{e}}_x$ with increasing distance from the cylinder. Naturally, a continuum of other basic modes fulfills the same purpose. The above choice has the advantage of its analytical simplicity.

The generalization of the GM to oncoming flows with more general 2-D or 3-D nonuniformities is obvious. Also in these cases, only the basic mode needs to be modified.

B. Circular cylinder in time-periodic flow

The GM can also be employed to a circular cylinder in uniform, time-periodic flow, $\mathbf{u}=(1+a\cos\omega t)\hat{\mathbf{e}}_x$, with the mean component of unity, the amplitude of the periodic component a, and the circular frequency ω. Like in Sec. VI A, only the original basic mode has to be changed. A proper choice is given by

$$\Psi_0=(1+a\cos\omega t)\left(r-\frac{1}{r}\right)\left[1-\exp\left(-\frac{r-1}{\delta_{bm}}\right)\right]\sin\phi.$$

For large amplitudes a, the asymptotic wake laws used for the derivation of the Hilbert-space parameter α are not valid anymore. In this case, another value of α has to be computed from similar considerations.

Naturally, the GM may be generalized for a large variety of nonuniform and unsteady oncoming flows.

C. Flow around a sphere

The flow around a sphere is described in a spherical coordinate system (r,ϕ,θ), where $r\geqslant 0$ represents the radial coordinate, $\phi\in[0,2\pi]$ the circumferential coordinate and $\theta\in[0,\pi]$ the azimuthal coordinate. The corresponding unit vectors are denoted by $\hat{\mathbf{e}}_r$, $\hat{\mathbf{e}}_\phi$, and $\hat{\mathbf{e}}_\theta$. In this system, the sphere is supposed to be described by $r=1$ and the flow has a velocity 1 in the direction of the ray $\theta=0$ (north pole).

As a basic mode we take, in analogy to the cylinder flow, the product of the potential solution and a factor accounting for viscosity

$$\Psi_0=\frac{1}{2}\sin^2\theta\left(r^2-\frac{1}{r}\right)\left[1-\exp\left(-\frac{r-1}{\delta_{bm}}\right)\right]$$

with a properly chosen scale δ_{bm}. This mode fulfills the no-slip condition at the sphere and converges to the ideal flow at infinity.

For the perturbation $\mathbf{u}'=\mathbf{u}-\mathbf{u}_0$ the carrier field $\hat{\mathbf{e}}_z$ in Zebib's[10] ansatz for the incompressible velocity field has to be replaced by $\hat{\mathbf{e}}_\phi$. Then the flow can be expressed in terms of the generalized streamfunctions $\Psi^{(\kappa)}$ $(\kappa=1,2)$:

$$\begin{aligned}\mathbf{u}'&=\nabla\times(\Psi^{(1)}\hat{\mathbf{e}}_\phi)+\nabla\times\nabla\times(\Psi^{(2)}\hat{\mathbf{e}}_\phi)\\&=\left[\frac{1}{r}\left(\frac{\partial}{\partial\theta}+\cot\theta\right)\Psi^{(1)}+\frac{1}{r\sin\theta}\left(\frac{\partial^2}{\partial r\partial\phi}+\frac{1}{r}\frac{\partial}{\partial\phi}\right)\Psi^{(2)}\right]\hat{\mathbf{e}}_r\\&\quad+\left[-\left(\frac{\partial}{\partial r}+\frac{1}{r}\right)\Psi^{(1)}+\frac{1}{r^2\sin\theta}\times\left(\frac{\partial^2}{\partial\theta\partial\phi}+\cot\theta\frac{\partial}{\partial\phi}\right)\Psi^{(2)}\right]\hat{\mathbf{e}}_\theta-\left[\left(\frac{\partial^2}{\partial r^2}+\frac{2}{r}\frac{\partial}{\partial r}\right.\right.\\&\quad\left.\left.-\frac{1}{r^2\sin^2\theta}+\frac{1}{r^2}\frac{\partial^2}{\partial\theta^2}+\frac{\cot\theta}{r^2}\frac{\partial}{\partial\theta}\right)\Psi^{(2)}\right]\hat{\mathbf{e}}_\phi.\end{aligned}\tag{25}$$

It may be worthwhile to note that the ϕ component of $\mathbf{u}'$ differs from the 3-D Laplacian of $\Psi^{(2)}$ only by term $(1/r^2\sin^2\theta)\Psi^{(2)}$ instead of $(1/r^2\sin^2\theta)(\partial^2\Psi^{(2)}/\partial\phi^2)$. The no-slip condition at the sphere is enforced by requiring $(\partial^i/\partial r^i)\Psi^{(\kappa)}=0$ for $i=0,1,\ldots,\kappa$.

The inner product for the generalized streamfunctions in the domain $\Omega=\{(r,\phi,\theta):\ r\geqslant 1\}$ may be defined in analogy to Eq. (7)

$$(f,g)_\Omega=\int_1^\infty dr\int_{-\pi}^{+\pi}d\phi\int_0^\pi d\theta\, r^{-\alpha}r^2\sin\theta fg,$$

where the Hilbert-space parameter α has to be determined as in the cylinder case. In this integral, $r^2 \sin\theta\, dr\, d\phi\, d\theta$ represents the volume element. The expansion modes are obtained by a product ansatz

$$\mathbf{u}_{ijk}^{(\kappa)} = (\nabla\times)^{\kappa}\{\Psi_{ijk}^{(\kappa)}\hat{\mathbf{e}}_{\phi}\}$$

with

$$\Psi_{ijk}^{(\kappa)} = R_i^{(\kappa)}(r)\Phi_j(\phi)\Theta_k^{(\kappa)}(\theta).$$

In this ansatz, the *radial modes* are the CCONS of the weighted Hilbert space $\mathscr{L}^2_{\sigma_{\mathscr{R}}}$ where the weight $\sigma_{\mathscr{R}} = r^{2-\alpha}$ is the radial factor of the product in $(f,g)_{\Omega}$. In analogy to the derivation of Eq. (10), we obtain

$$R_i^{(\kappa)} = \frac{1}{\sqrt{\delta^{(\kappa)}}}\, r^{(\alpha-2)/2}\left(\frac{r-1}{\delta^{(\kappa)}}\right)^{\kappa+1} P_i^{(\kappa)}\left(\frac{r-1}{\delta^{(\kappa)}}\right) \times \exp\left[-\left(\frac{r-1}{2\delta^{(\kappa)}}\right)\right],$$

where the $\delta^{(\kappa)}$ is to be computed from estimates for the boundary-layer thickness and $P_i^{(\kappa)}$ represents a polynomial of degree i, whose coefficients are calculated from a successive Gram–Schmidt orthonormalization of $R_0^{(\kappa)}$, $R_1^{(\kappa)}$, etc.

The *circumferential modes* $\Phi_j(\phi)$ are expressed by Eq. (13).

The *azimuthal modes* are defined by

$$\Theta_k^{(\kappa)}(\theta) = (\sin\theta)^{\kappa}\begin{cases}\sin(2k\theta) & \text{for } k>0,\\ \cos(2k\theta) & \text{for } k\leqslant 0.\end{cases}$$

The factor $(\sin\theta)^{(\kappa)}$ guarantees that the velocity field $\mathbf{u}_{ijk}^{(\kappa)}$ has no singularities on the north–south axis. The other factor is the complete orthogonal system for the π-periodic functions. It should be noted that the orthonormalization of the azimuthal modes must be carried out with respect to the $\sin\theta$ weight of the inner product $(f,g)_{\Omega}$.

For all indices (κ,i,j,k) with $\kappa=1, 2$, $i\geqslant 0$, and j, $k=0, \pm 1, \pm 2,\ldots$, the expansion modes $\mathbf{u}_{ijk}^{(\kappa)}$ are smooth functions in the domain $0<\theta<\pi$. In addition, an inspection of Eq. (25) reveals that they have no discontinuities of the second kind (singularities) on the north–south axis ($\theta=0$ or π). Yet, a careful analysis yields that there exists a group of modes ($k\leqslant 0$ and $j=0, \pm 2, \pm 4,\ldots$) which has discontinuities of the first kind (finite jumps) on this axis. This group has to be excluded from the index set.

The present GA is expected to describe the flow arbitrarily exactly with sufficiently many modes. Yet, the completeness cannot be simply proven with elementary functional analysis because of the $\sin\theta$ factor in the inner product $(f,g)_{\Omega}$. Orthonormality can, in principle, be achieved with the Gram–Schmidt procedure. This specifies the GA for the velocity field.

The evolution equations for the generalized streamfunctions can be derived in analogy to the cylinder case, replacing $\hat{\mathbf{e}}_z$ by $\hat{\mathbf{e}}_{\phi}$ in Zebib's derivation. This results in similar equations. The GP to an AS of the form (24) is then a straightforward task.

D. Boundary-layer flow

The boundary layer over a flat plate is most naturally described in a Cartesian coordinate system (x,y,z), where the x axis is aligned with the direction of the mean flow, and y is the distance from the plate. If one is only interested in the simulation of local events (burst, sweeps, ejections, hairpin vortices), the growth of the displacement thickness δ_1 in mean-flow direction may be neglected. The basic mode is defined by

$$\mathbf{u}_0 = \nabla\times(\Psi_0\hat{\mathbf{e}}_z)$$

with

$$\Psi_0 = y-(1-e^{-y/\delta_1})/\delta_1.$$

The corresponding velocity field has the exponential profile $\mathbf{u}_0=[1-\exp(-y/\delta_1)]\,\hat{\mathbf{e}}_x$.

For the perturbation $\mathbf{u}'=\mathbf{u}-\mathbf{u}_0$, we assume an L_x periodicity in mean-flow direction and an L_z periodicity in spanwise direction as in the simulations of other authors. The perturbation can be expressed by

$$\begin{aligned}\mathbf{u}' &= \nabla\times(\Psi^{(1)}\hat{\mathbf{e}}_z)+\nabla\times\nabla\times(\Psi^{(2)}\hat{\mathbf{e}}_z)\\ &= \left(\frac{\partial\Psi^{(1)}}{\partial y}+\frac{\partial^2\Psi^{(2)}}{\partial x\partial z}\right)\hat{\mathbf{e}}_x+\left(-\frac{\partial\Psi^{(1)}}{\partial x}+\frac{\partial^2\Psi^{(2)}}{\partial y\partial z}\right)\hat{\mathbf{e}}_y\\ &\quad -\Delta_{2D}\Psi^{(2)}\hat{\mathbf{e}}_z,\end{aligned} \tag{26}$$

where $\Delta_{2D}=\partial^2/\partial x^2+\partial^2/\partial y^2$ is the 2-D Laplace operator. The no-slip condition is equivalent to requiring $(\partial^j/\partial y^j)\Psi^{(\kappa)}=0$ at the wall $y=0$ for $j=0,1,\ldots,\kappa$. The domain of the generalized streamfunctions $\Psi^{(\kappa)}$ can be restricted to $\Omega=\{(x,y,z):\ |x|\leqslant L_x/2, y>0,\ |z|\leqslant L_z/2\}$ because of the periodic boundary conditions. The inner product for f,g is defined by

$$(f,g)_{\Omega}=\int_{-L_x}^{+L_x}dx\int_0^{\infty}dy\int_{-L_z}^{+L_z}dz\, fg.$$

No weight has to be introduced to assure the finiteness of the norms $\|\Psi^{(\kappa)}\|_{\Omega}=\sqrt{(\Psi^{(\kappa)},\Psi^{(\kappa)})_{\Omega}}$, since the perturbations rapidly decay with increasing distance from the wall. The inner product and the boundary conditions suggests to construct the expansion modes in terms of trigonometric modes $X_i(x)$ and $Z_k(z)$ and Laguerre-type modes $Y_j^{(\kappa)}(y)=(y/\delta_1)^{\kappa}P_j^{(\kappa)}(y/\delta_1)\exp(-y/2\delta_1)$, where $P_j^{(\kappa)}$ is a polynomial of jth order:

$$\mathbf{u}_{ijk}^{(\kappa)}=(\nabla\times)^{\kappa}\Psi_{ijk}^{(\kappa)}\hat{\mathbf{e}}_z$$

with

$$\Psi_{ijk}^{(\kappa)}=X_i(x)\,Y_j^{(\kappa)}(y)Z_k(z).$$

Possibly κ-dependent scales $\delta^{(\kappa)}$ for the Y modes may significantly accelerate the convergence of the GM with increasing number of modes.

The evolution equations are given by Eqs. (21) and (22), noting that the 2-D and 3-D Laplacians, Δ_{2D} and Δ, must be expressed in Cartesian coordinates and the factor

of 2 in the dissipation term is to be omitted. In addition, the Reynolds number is now to be defined by $\mathrm{Re}=\mathrm{Re}_\delta=U_\infty\delta_1/\nu$.

With the above information, the GP is a straightforward computation and the GM is uniquely defined.

E. Channel flow

The channel flow is described in a Cartesian coordinate system (x,y,z), where the channel walls are given by $y=\pm 1$ and the x-axis points in the direction of the mean flow. As a basic mode the steady solution

$$\mathbf{u}_0=\nabla\times(\Psi_0\hat{\mathbf{e}}_z)$$

with

$$\Psi_0=\tfrac{3}{2}(y-\tfrac{1}{3}y^3),$$

with the parabolic velocity profile $\mathbf{u}_0=u_0\hat{\mathbf{e}}_x=\frac{3}{2}(1-y^2)\hat{\mathbf{e}}_x$ is most suitable. This basic mode is normalized to yield $\frac{1}{2}\int_{-1}^{+1}dy\,u_0=1$.

The Hilbert space and the expansion modes are chosen as in Sec. VI D except that the domain for y is now finite, $[-1,+1]$, and the Y modes are replaced by $Y_j^{(\kappa)}=(1-y^2)^\kappa P_j^{(\kappa)}(y)$, $P_j^{(\kappa)}$ being a polynomial of degree j. The evolution equation for the generalized streamfunction has also the same form, the Reynolds number being defined in terms of the mean velocity and half the channel width.

F. Pipe flow

The flow in a circular pipe is described in cylindrical coordinates (r,ϕ,z), where the cylinder is specified by $r=1$. The steady solution of the Navier–Stokes equation

$$\mathbf{u}_0=\nabla\times\nabla\times\{\Psi_0\hat{\mathbf{e}}_z\}$$

with

$$\Psi_0=2\left[\left(\frac{r}{2}\right)^2-\left(\frac{r}{2}\right)^4\right]$$

is taken as the basic mode. Note that the curl is now applied two times. The corresponding velocity profile in z direction is $w=2(1-r^2)$, i.e., the velocity averaged over the cross section, $(1/\pi)\int_0^1 dr\int_{-\pi}^{+\pi}d\phi\,2\pi rw$, is unity.

The perturbation can be expressed by Eq. (3) with the same no-slip condition. Assuming an L_z periodicity in mean-flow direction, the domain for the dependent variables can be restricted to $\Omega=\{(r,\phi,z)\colon r\leqslant 1,|z|\leqslant L_z/2\}$. The inner product for the generalized streamfunctions is defined by $(f,g)_\Omega=\int_\Omega dV\,fg$, where $dV=2\pi\,dr\,d\phi\,dz$ is an infinitesimal volume element. The canonical choice for the expansion modes is

$$\mathbf{u}_{ijk}^{(\kappa)}=(\nabla\times)^\kappa\{\Psi_{ijk}^{(\kappa)}\hat{\mathbf{e}}_z\}$$

with

$$\Psi_{ijk}^{(\kappa)}=R_i^{(\kappa)}(r)\Phi_j(\phi)Z_k(z).$$

The *circumferential* and *axial* modes, Φ_j and Z_k, are 2π and L_z-periodic Fourier modes. The *radial modes* $R_i^{(\kappa)}$ are given by linear combinations of Bessel functions of the first kind:

$$R_i^{(\kappa)}=\sum_{\alpha=0}^{i+\kappa-1}c_{\alpha,i}^{(\kappa)}J_0(k_{0i}r),$$

where k_{0i} is the ith zero of J_0 and the coefficients $c_{\alpha,i}^{(\kappa)}$ are computed with a Gram–Schmidt orthonormalization procedure taking into account the no-slip condition at the pipe walls.

The equation of motion for the generalized streamfunctions $\Psi^{(\kappa)}$ $(\kappa=1,2)$ is given by Eqs. (21) and (22) with another definition for the Reynolds number. The Galerkin projection (GP) may be carried out as in Sec. II B. The resulting AS has a vanishing constant term, since the basic mode is a steady solution of the Navier–Stokes equation.

G. Taylor–Couette flow

From the previous examples, it is clear that the Taylor–Couette flow can also be described with the GM presented in this paper. This flow is most naturally described in a cylindrical coordinate system (r,ϕ,z), where the outer and inner cylinder are given by $r=1$ and $r=r_0<1$, respectively. The basic mode is taken to be the 1-D steady solution

$$\mathbf{u}_0=\nabla\times\{\Psi_0\hat{\mathbf{e}}_z\}$$

with

$$\Psi_0=\tfrac{1}{2}ar^2+b\log r.$$

The constants a and b are functions of the angular velocities and the radii of the inner and outer cylinder.[41]

The perturbation $\mathbf{u}'=\mathbf{u}-\mathbf{u}_0$ is expressed by Eq. (3) and is assumed to have an L_z periodicity in z direction. The expansion modes $\Psi_{ijk}^{(\kappa)}$ are factorized in z *modes* given by Eq. (17), in *azimuthal modes* [Eq. (14)] and in *radial modes* which are suitable linear combinations of Bessel functions satisfying the no-slip conditions at $r=r_0$ and $r=1$. Now, the Galerkin approximation and projection can be carried out in complete analogy to the cylinder flow.

H. More complex boundary conditions

All above examples possess translation- or rotation-invariant boundary conditions. This symmetry simplifies the analytic calculations for the GM, but this is not necessary for the applicability. The symmetry is replaced by much weaker requirements. Suppose that (ζ,η,χ) is a locally orthogonal coordinate system. The flow is confined in a domain Ω which is bounded by one or two boundaries. These boundaries are described by $\eta=\text{const}$. Infinity is also considered as the "boundary" $\eta=\infty$. Then, the corresponding velocity field can be expressed by Eq. (3) with the local unit vector $\hat{\mathbf{e}}_\zeta$ or $\hat{\mathbf{e}}_\chi$ instead of $\hat{\mathbf{e}}_z$. The no-slip condition at the surface is given by $(d^j/d\eta^j)\Psi^{(\kappa)}=0$ for $j=0,1,\ldots,\kappa$. The inner product for the generalized streamfunctions is defined by $(f,g)=\int_\Omega dV\,\sigma fg$, where σ is unity or a position-dependent weight. One problem that may arise is that the factor $\sigma\,dV$ does not separate as a product of the form $F(\xi)G(\eta)H(\chi)d\xi\,d\eta\,d\chi$. Then, either the orthonormality requirement for the product ex-

pansion modes $\Psi_{ijk}^{(\kappa)}=X_i^{(\kappa)}(\zeta)Y_j^{(\kappa)}(\zeta)Z_k^{(\kappa)}(\chi)$ must be dropped or the weight σ must be chosen in a form which factorizes $\sigma\,dV$ as product of differentials in ζ, η, and χ. The evolution equations for the generalized streamfunctions is derived in analogy to Zebib's calculations[10] replacing $\hat{\mathbf{e}}_z$ by $\hat{\mathbf{e}}_\zeta$ or $\hat{\mathbf{e}}_\chi$. With these guidelines, the GM for the flow around ellipsoids and elliptical cylinders can be carried out with well-known coordinate systems. For more complex boundary conditions, the construction of suitable coordinate systems may be difficult.

VII. CONCLUSION

In the present paper, guidelines for the construction of successful Galerkin methods are given. The construction of the basic mode, which shall remove the inhomogeneity of the boundary conditions, turns out to be uncritical. Yet, the choice of the Hilbert space for the remaining perturbation may be crucial. The Hilbert space should contain the asymptotic solution, but it should, on the other hand, not be much larger. In particular, the space of square-integrable functions, on which most mathematical Galerkin methods for confined flows are based on, may be too small for open, unconfined flows. Similarly, the freedom of constructing complete sets of expansion modes in the Hilbert space may strongly affect the Galerkin solutions. This freedom should be exploited to guarantee that the Galerkin representation of the dissipative and convective term is of similar order of magnitude. For the cylinder wake, this can be achieved with boundary-layer scaled radial modes. Although the above guidelines have only been developed for one Galerkin method which is applied to one flow problem, they are, once discovered, almost self-evident and may be expected to be valid for most other low-dimensional flow descriptions.

Considering these aspects, a Galerkin method for the 3-D cylinder wake is constructed. This method yields reasonable solutions with less than 200 global modes. As to the authors' knowledge, this is the first low-dimensional, *a priori* simulation of an unsteady wake flow which does not require detailed empirical knowledge about the flow properties. For the present Galerkin method, only rough estimates for the boundary-layer thickness and the asymptotic wake laws are employed. With proper-orthogonal-decomposition (POD) techniques, which incorporate numerical transient solutions, the number of necessary modes for the 2-D, periodic wake can be even further reduced.[38] This POD investigation confirms also the necessity of introducing Reynolds-number-dependent modes.

The generalization of the presented Galerkin method has been outlined for a variety of flow problems. This method is particularly suited for 3-D global stability analyses for steady and periodic flows, which cannot be carried out using finite-difference or finite-element methods with the presently available computer power. Thus the first 3-D global stability investigation of the steady and periodic flow around a circular cylinder could be performed with our method, yielding results which are in good agreement with experiments.[6,27] Furthermore, the Galerkin method is well suited for the analysis of the turbulence attractor. Experimentally obtained reconstructed attractors of the turbulent cylinder wake showed the importance of high-dimensional processes for the small-scale fluctuations.[30,31] For the turbulence modeling purposes, the decomposition of the temporal behavior in a low-dimensional dynamics and these stochastic fluctuations would be of large interest. Corresponding investigations of the theoretical cylinder-wake attractor with POD techniques, localized Lyapunov exponents, etc., are in progress. (See, for instance, Ref. 37.)

The presented Galerkin method is a numerically efficient technique for flows with simple geometries and can provide physical insights which can hardly be extracted from the more accurate and flexible finite-difference and finite-element solvers.

ACKNOWLEDGMENTS

The authors are indebted to Professor E.-A. Müller for his continuous interest in the progress of the work and for providing an ideal research environment. We are particularly grateful to R. Nolte for many fruitful discussions and for his critical comments to the present manuscript. We acknowledge stimulating discussions with Dr. U. Dallmann, Dr. L. Kleiser, Dr. W. Koch, and Dr. W. Möhring, who contributed to the presented results with constructive advices.

APPENDIX: CONSTRUCTION OF THE HILBERT SPACE

In the following, the borderline Hilbert-space parameter α_{crit} is determined. As reasoned in Sec. II A, there exists a Hilbert-space parameter α_{crit} below which the norm $\|f\| = \sqrt{(f,f)_\Omega}$ of at least one of the generalized streamfunctions $\Psi^{(\kappa)}$ for the asymptotic (steady, periodic, and turbulent) solution diverges and above which these norms are well defined, i.e., converge.

The determination of the critical parameter requires some knowledge about the asymptotic solution. It turns out that the well known far-wake asymptotics suffice. In particular, we use that the width of the laminar and turbulent wake behind an arbitrarily shaped cylinder b increases proportionally to $\sqrt{x}$, while the wake defect $a:=u-U_\infty$ on the $\phi=0$ ray decreases proportionally to $1/\sqrt{x}$. In addition, it is employed that the intensity of turbulent fluctuations decreases proportionally to $1/x$, since turbulence decays with the inverse distance of its origin. The characteristic variation of the generalized streamfunctions in the wake region is denoted by $\delta\Psi^{(\kappa)}$ ($\kappa=1,2$). The contribution of the basic mode to the flow in the wake can be identified with the uniform flow $\mathbf{u}_\infty=U_\infty\,\hat{\mathbf{e}}_x$, since $\mathbf{u}_\infty-\mathbf{u}_0$ is of the order $O(r^{-2})$.

First, $\Psi^{(1)}$ is considered. The wake defect $a(x)=(\partial/\partial y)\Psi^{(1)}$ can be estimated by $\delta\Psi^{(1)}/b(x)$. Since $a\sim O(x^{-1/2})$ and $b\sim O(x^{1/2})$, we obtain $\delta\Psi^{(1)}\sim O(x^0)$. Taking $\delta\Psi^{(1)}$ as a measure of $\Psi^{(1)}$, it can be concluded that $\Psi^{(1)}$ is uniformly bounded but does not decay with increas-

ing x. Outside the wake, $\Psi^{(1)}$ is neglected, because there no infinite contribution to the norm integral for $\|\Psi^{(1)}\|_\Omega$ can be expected. Hence, the norm converges if and only if the integral $\int_{-L/2}^{L/2} dz \int_{\text{wake}} dA r^{-\alpha}\ (\Psi^{(1)})^2$ converges, where dA is the infinitesimal area element $2\pi r\, dr\, d\phi$ in the wake region. Due to $(\Psi^{(1)})^2 \sim O(x^0)$ and the parabolic shape of the wake region, $\|\Psi^{(1)}\|_\Omega < \infty$ is equivalent to $\alpha > 3/2$. Therefore, $\alpha_{\text{crit}} \geqslant 3/2$.

Finally, similar considerations for $\Psi^{(2)}$ are carried out. The spanwise velocity component w is only a function of $\Psi^{(2)}$ and does not depend on Ψ_0 or $\Psi^{(1)}$. According to Eq. (3), $w = -(\partial^2/\partial x^2 + \partial^2/\partial y^2)\ \Psi^{(2)}$. Since the x variations in the wake are generally small with respect to the y variation, the w component is, by dimensional arguments, of the order of $\delta\Psi^{(2)}/b^2$. Exploiting $b^{-2} \propto 1/x$ and $w \propto 1/x$, we also get for the second generalized streamfunction $\Psi^{(2)} \sim O(x^0)$. Therefore, *both* functions can be expected to have diverging norms for $\alpha < 3/2$ and finite, well-defined norms for $\alpha > 3/2$. The critical Hilbert-space parameter is hence given by

$$\alpha_{\text{crit}} = \tfrac{3}{2}.$$

Two remarks are in order. First, the above reasoning can be made more precise by separately discussing the mean and fluctuating contribution of Ψ_0 and $\Psi^{(\kappa)}$ $(\kappa = 1,2)$ to the velocity field inside and outside the wake and estimating the corresponding decay laws. These more precise arguments yield the same result. Since such a case by case discussion is very lengthy, it has been avoided for reasons of clarity.

Second, the norms of the generalized streamfunctions converge only for $\alpha > 3/2$ and not for $\alpha = 3/2$. Mathematically, this implies that a suitable Hilbert-space parameter must be of the form $\alpha = 3/2 + \epsilon$, where ϵ is an arbitrarily small positive quantity. Numerically, however, the present GM is insensitive to this $\epsilon \ll 1$, since its expansion modes decay exponentially with the distance from the cylinder. Hence, we set $\epsilon = 0$.

[1] C. A. J. Fletcher, *Computational Galerkin Methods* (Springer-Verlag, New York, 1984), p. 30.

[2] N. Aubry, P. Holmes, J. L. Lumley, and E. Stone, "The dynamics of coherent structures in the wall region of a turbulent boundary layer," J. Fluid Mech. **192**, 115 (1988).

[3] X. Zhou and L. Sirovich, "Coherence and chaos in a model of turbulence boundary layer," Phys. Fluids A **4**, 2855 (1992).

[4] D. Rempfer, "Kohärente Strukturen und Chaos beim laminar-turbulenten Grenzschichtumschlag," Ph.D. thesis, Fakultät Verfahrenstechnik der Universität, Stuttgart, 1991.

[5] L. Boberg and U. Brosa, "Onset of turbulence in a pipe," Z. Naturforsch. **43a**, 697 (1988).

[6] B. R. Noack and H. Eckelmann, "Theoretical investigation of the cylinder wake with a low-dimensional Galerkin method," in *IUTAM-Symposium on Bluff Body Wakes, Dynamics and Instability*, edited by H. Eckelmann, J. M. R. Graham, P. Huerre, and P. A. Monkewitz (Springer-Verlag, Berlin, 1993), pp. 143–146.

[7] E. N. Lorenz, "Deterministic nonperiodic flow," J. Atmos. Sci. **20**, 130 (1963).

[8] G. E. Karniadakis (personal communication, 1992).

[9] J. L. Lumley, *Stochastic Tools in Turbulence* (Academic, New York, 1970).

[10] A. Zebib, "Stability of viscous flow past a circular cylinder," J. Eng. Math. **21**, 155 (1987).

[11] B. R. Noack and H. Eckelmann, "On chaos in wakes," Physica D **56**, 151 (1992).

[12] B. R. Noack and H. Eckelmann, "Two-dimensional, viscous, incompressible flow around a circular cylinder," Max-Planck-Institut für Strömungsforschung, Report No. 104/1991, Göttingen, 1991.

[13] G. E. Karniadakis and G. S. Triantafyllou, "Three-dimensional dynamics and transition to turbulence in the wake of bluff bodies," J. Fluid Mech. **238**, 1 (1992).

[14] A. G. Tomboulides, G. S. Triantafyllou, and G. E. Karniadakis, "A mechanism of period doubling in free shear flows," Phys. Fluids A **4**, 1329 (1992).

[15] V. A. Patel, "Kármán vortex street behind a circular cylinder by series truncation method," J. Comput. Phys. **28**, 14 (1978).

[16] F. S. Acton, *Numerical Methods That Work* (Harper and Row, New York, Evanston, 1970), p. 130.

[17] B. R. Noack, "Theoretische Untersuchung der Zylinderumströmung mit einem niedrigdimensionalen Galerkin-Verfahren," Max-Planck-Institut für Strömungsforschung, Report No. 25/1992, Göttingen, 1992.

[18] M. Van Dyke, *Perturbation Methods in Fluid Mechanics* (Parabolic, Stanford, 1975), p. 150 (annotated edition).

[19] B. Fornberg, "A numerical study of steady viscous flow past a circular cylinder," J. Fluid Mech. **98**, 819 (1980).

[20] P. J. Strykowski and K. Hannemann, "Temporal simulation of the wake behind a circular cylinder in the neighborhood of the critical Reynolds number," ACTA Mech. **90**, 1 (1991).

[21] K. R. Sreenivasan, P. J. Strykowski, and D. J. Olinger, "Hopf bifurcation, Landau equation, and vortex shedding behind circular cylinders," in *Forum on Unsteady Flow Separation*, Fluids Engineering Division Vol. 52, edited by K. N. Ghia (American Society for Mechanical Engineers, New York, 1987), p. 1.

[22] C. H. K. Williamson, "Oblique and parallel modes of vortex shedding in the wake of a circular cylinder at low Reynolds numbers," J. Fluid Mech. **206**, 579 (1989).

[23] C. P. Jackson, "A finite-element study of the onset of vortex shedding in flow past variously shaped bodies," J. Fluid Mech. **182**, 23 (1987).

[24] M. Provansal, C. Mathis, and L. Boyer, "Bénard–von Kármán instability: transient and forced regimes," J. Fluid Mech. **182**, 1 (1987).

[25] A. Roshko, "On the drag and shedding frequency of two-dimensional bluff bodies," NACA Report No. 3169, Washington, D.C., 1954.

[26] C. H. K. Williamson, "The existence of two stages in the transition to three dimensionality of a cylinder wake," Phys. Fluids **31**, 3165 (1988).

[27] B. R. Noack, M. König, and H. Eckelmann, "Three-dimensional stability analysis of the periodic flow around a circular cylinder," Phys. Fluids A **5**, 1279 (1993).

[28] M. König, H. Eisenlohr, and H. Eckelmann, "The fine structure in the Strouhal–Reynolds number relationship of the laminar wake of a circular cylinder," Phys. Fluids A **2**, 1607 (1990).

[29] C. H. K. Williamson, "Defining a universal and continuous Strouhal–Reynolds number relationship for the laminar vortex shedding of a circular cylinder," Phys. Fluids **31**, 2742 (1988).

[30] B. R. Noack, "Untersuchung chaotischer Phänomene in der Nachlaufströmung," Max-Planck-Institut für Strömungsforschung, Report No. 111/1990, Göttingen, 1990.

[31] B. R. Noack and F. Obermeier, "A chaos-theoretical investigation of the wake behind a cylinder," Z. Angew. Math. Mech. **71**, T259 (1991).

[32] D. Rempfer, "Low-dimensional modes of a flat-plate boundary layer," in *Near-Wall Turbulent Flows*, edited by R. M. C. So, C. G. Speziale, and B. E. Launder (Elsevier, Amsterdam, 1993), pp. 63–72.

[33] L. Sirovich, "Chaotic dynamics of coherent structures," Physica D **37**, 561 (1989).

[34] O. A. Ladyzhenskaya, *The Mathematical Theory of Viscous Incompressible Flow* (Gordon and Breach, New York, 1963), p. 155.

[35] G. E. Karniadakis, "Spectral element simulations of laminar and turbulent flows in complex geometries," Appl. Numer. Math. **6**, 85 (1989/1990).

[36] M. König, B. R. Noack, and H. Eckelmann, "Descrite shedding modes in the von Kármán vortex street," Phys. Fluids A **5**, 1846 (1993).

[37] B. R. Noack and H. Eckelmann, "Theoretical investigation of the bifurcations and the turbulence attractor of the cylinder wake," to appear in Z. Angew. Math. Mech.

[38] A. E. Deane, I. G. Kevrekidis, G. E. Karniadakis, and S. A. Orszag, "Low-dimensional models for complex geometry flows: Application to

grooved channels and circular cylinders," Phys. Fluids A **3**, 2337 (1991).
[39]B. R. Noack and H. Eckelmann, "A Galerkin study of the cylinder wake," Max-Planck-Institut für Strömungsforschung, Report No. 101/1991, Göttingen, 1991.
[40]A. G. Tomboulides, M. Israeli, and G. E. Karniadakis, "Viscous-sponge outflow condition for incompressible flows," Mini-symposium on Outflow Boundary Conditions, Stanford, August 1991.
[41]L. D. Landau and E. M. Lifshitz, *Fluid Mechanics, Course of Theoretical Physics* (Pergamon, Oxford, 1987), Vol. 6, p. 56.